HIGHER ORDER DISCONTINUOUS FINITE ELEMENT METHODS FOR

DISCRETE ORDINATES THERMAL RADIATIVE TRANSFER

A Dissertation

by

PETER GREGORY MAGINOT

Submitted to the Office of Graduate and Professional Studies of
Texas A&M University
in partial fulfillment of the requirements for the degree of

DOCTOR OF PHILOSOPHY

Co-Chairs of Committee,	Jim E. Morel
	Jean C. Ragusa
Committee Members,	Marvin L. Adams
	Jean-Luc Guermond
Head of Department,	Yassin A. Hassan

May 2015

Major Subject: Nuclear Engineering Department

ABSTRACT

Lorem ipsum dolor sit amet, consectetur adipiscing elit. Integer lectus quam, condimentum quis bibendum eu, sollicitudin eget lacus. Praesent non sodales odio. Class aptent taciti sociosqu ad litora torquent per conubia nostra, per inceptos himenaeos. Nulla ac luctus sapien. Morbi cursus sapien eget lorem fermentum hendrerit. Nam ac erat dui, in cursus velit. Vivamus hendrerit porttitor nisi, ut porttitor lorem volutpat eget. In ligula ligula, euismod ut condimentum sit amet, pulvinar sit amet diam. Pellentesque interdum, ipsum ullamcorper consequat dignissim, sem arcu egestas mauris, vitae interdum sem tortor ut ante. Nunc blandit laoreet nisi, non rutrum lorem hendrerit quis. Cras nunc diam, convallis et feugiat at, auctor id libero. Nunc facilisis massa eu eros imperdiet vestibulum. Vestibulum ante ipsum primis in faucibus orci luctus et ultrices posuere cubilia Curae; Donec non velit vitae tortor blandit semper.

Etiam vitae dolor nulla. Ut eros odio, rhoncus eget placerat vitae, elementum ac ante. Proin vitae odio eu nisl pharetra mattis. Pellentesque habitant morbi tristique senectus et netus et malesuada fames ac turpis egestas. Phasellus fermentum lacus consectetur neque consequat ullamcorper. Cras blandit urna non dui consequat molestie. Curabitur viverra nibh at nisi semper faucibus. Nam egestas mauris a enim dignissim nec consectetur tortor rutrum. Mauris at nisi in est luctus congue ut mattis est. Ut pretium, mi quis elementum cursus, ante eros suscipit ligula, ut porttitor elit leo sed turpis. Nam sed dui ligula.

DEDICATION

To my wife, Kelli, for traveling with me along all the unforeseen curves of life. To my mom and dad, for providing my foundation and inspiration.

ACKNOWLEDGEMENTS

NOMENCLATURE

B/CS   Bryan/College Station

HSUS   Humane Society of the United States

P   Pressure

T   Time

TVA   Tennessee Valley Authority

TxDOT   Texas Department of Transportation

This page is optional.

TABLE OF CONTENTS

LIST OF FIGURES

LIST OF TABLES

1. INTRODUCTION

This dissertation is dedicated to the solution of thermal radiative transfer (TRT) equations. The TRT equations:

$$\frac{1}{c}\frac{dI}{dt} + \vec{\Omega}\cdot\vec{\nabla}I + \sigma_t I = \int_0^\infty \int_{4\pi} \sigma_s(\vec{\Omega}' \to \vec{\Omega}, E' \to E)I\,d\vec{\Omega}'dE' + \sigma_a B \quad (1.1a)$$

$$C_v\frac{dT}{dt} = \int_0^\infty \sigma_a\,(\phi - 4\pi B)\,dE\,, \quad (1.1b)$$

are a nonlinear system of equations that describe the exchange of energy between a photon radiation field and a non-moving material. The radiation intensity, I, is a seven dimensional field dependent upon spatial location, $\vec{x}$; photon energy, E; photon direction of travel, $\vec{\Omega}$; and time t. c is the speed of light. Material opacities for all interactions, σ_t; absorption, σ_a; and scattering, σ_s are functions of photon energy and material temperature, T. Material heat capacity, C_v, is also a function of material temperature. The angle integrated radiation intensity is an integral over all photon directions of the the photon intensity and is a function of space and photon energy. Finally, the Planck function, B, is a function of photon energy and material temperature. While materials at all temperatures emit photon radiation, the radiation emission is proportional to T^4. Thus, solution of the radiative transfer equations is most important in situations where materials are very hot. Solving the thermal radiative transfer equations is an important component of the simulation of different scientific and engineering problems including astrophysics supernova explosions and high energy density laboratory physics experiments like those conducted at the National Ignition Facility.

1.1 Simplifications of the Thermal Radiative Transfer Equations

In this dissertation, we we make a number of simplifying assumptions to make solution of Eqs. (1.1) more tractable. First, we limit our focus to 1-D Cartesian (slab) geometry. The assumption of slab geometry is not required, but slab geometry radiation transport simulations require significantly less computational time. Further, any methods that have a possibility of being viable for radiation transport in multiple spatial dimensions must also work well in slab geometry.

Second, we approximate the continuous angle dependence of the intensity using the discrete ordinates (S_N) method. The S_N method approximates the true definition of the angle integrated intensity,

$$\phi(\vec{x}, E, t) = \int_{4\pi} I(\vec{x}, \vec{\Omega}, E, t) d\vec{\Omega},$$

using quadrature integration,

$$\phi(\vec{x}, E, t) \approx \sum_{d=1}^{N_{dir}} w_d I(\vec{x}, \vec{\Omega}_d, E, t). \tag{1.2}$$

In Eq. (1.2), $\{w_d, \vec{\Omega}_d\}_{d=1,...N_{dir}}$ is the set of N_{dir} quadrature weights w_d and discrete directions, $\vec{\Omega}_d$ and corresponding intensities I_d.

Finally, we treat the photon energy dependence using the multi-frequency method. The multi-frequency method approximates photon energy dependence by discretizing the continuous photon energy dependence with G discrete groups such that:

$$\int_0^\infty I(\vec{x}, \vec{\Omega}, t, E) dE = \sum_{g=1}^{G} I_g, \tag{1.3}$$

where

$$I(\vec{x}, \vec{\Omega}, t)_g = \int_{E_{g+1/2}}^{E_{g-1/2}} I(\vec{x}, \vec{\Omega}, t, E) dE \,, \qquad (1.4)$$

$E_{g+1/2}$ is the lower photon energy bound of group g, $E_{g-1/2}$ is the upper photon energy bound of group g, and we have maintained the traditional neutron transport number of higher energy particles belonging to lower number energy groups.

1.2 Spatial and Temporal Discretization

To complete a description of the approach we will take to solve Eqs. (1.1), we now describe how we will discretize the spatial and temporal variables.

1.2.1 Time Integration

The appearance of the speed of light in Eq. (1.1) results in the TRT equations being very stiff. To solve the such a stiff system of equations would require either an impractically small time step, or the use of implicit methods. We elect to use Diagonally Implicit Runge-Kutta (DIRK) methods to advance our TRT solution in time. The simplest of DIRK scheme is the first order implicit Euler scheme, but more advanced DIRK higher order methods in time [5].

1.2.2 Spatial Discretization with Discontinuous Finite Elements

The linear discontinuous finite element method (LDFEM) has long been used to solve the discrete ordinates neutron transport equation [22]. Through manipulation, the thermal radiative transfer equations can be transformed into a form that is equivalent to the neutron transport equation with pseudo- scattering, fission, and fixed sources. This makes it possible to use the same methods and techniques developed for neutron transport to assist in solving the thermal radiative transfer equations. LDFEM has achieved wide spread acceptance in the neutron transport community because it is accurate [12] and highly damped. Because it possesses the thick diffusion

limit [11], LDFEM has also been applied to the S_N TRT equations. Morel, Wareing, and Smith first considered the application of LDFEM to the S_N TRT equations in [18]. Mass matrix lumped LDFEM was shown to preserve the thick equilibrium diffusion limit [18]. This suggests that discontinuous finite element (DFEM) schemes can be used to accurately solve the TRT equations in both diffusive and transport effects dominated regions.

1.3   Progression Towards Higher Order DFEM Thermal Radiative Transfer

For higher order (quadratic and higher polynomial degree trial spaces) DFEM to be accurate and practical for solving Eqs. (1.1) we must demonstrate that higher order DFEM:

1. are "robust",

2. account for within cell spatial variation of opacity accurately, and

3. can be accelerated using appropriate iterative acceleration techniques.

By "robust", we mean that that calculated radiation outflow from a spatial cell is strictly positive for all cell widths and optical thicknesses.

In Section 2 we use a steady-state, mono-energetic, source-free pure absorber neutron transport problem with a cross section that is constant in space to examine the robustness of different radiation transport DFEM matrix lumping techniques. Next, we extend the techniques developed by Adams [2, 4], for a spatial discretization scheme related to LDFEM to address the within cell spatial variation of opacity, for higher order DFEM in Section 3 . Then, we examine iterative acceleration techniques compatible with higher order DFEM spatial discretizations that account for the spatial variation of interaction cross (in neutron transport problems) or opacity (TRT simulations) in Section 4.

4

In preparation for solving the coupled, non-linear TRT equations, in Section 5 we combine all of the strategies we have developed in Sections 2-4 and apply them to a coupled system of linear equations. Section 5, is deveoted to the development and solution of a two-group fuel depletion problem that uses explicit Euler time differencing. Finally, in Section 6 we solve the energy integrated, or grey, thermal radiative transfer equations using higher order DFEM. We then provides solutions to analytic benchmarks to verify our methods [26], and use the method of manufactured solutions [23] to demonstrate the increased accuracy of applying higher order DFEM and DIRK time integration techniques to the grey TRT equations.

2. DISCONTINUOUS FINITE ELEMENTS FOR RADIATION TRANSPORT

In Section 1, we briefly mentioned that through manipulation, the thermal radi-atve transfer equations can be put into a form equivalent to the neutron transport equation with pseudo- scattering, fission, and fixed sources. We will (repeatedly) go through this process in Section 6, but for now we take for granted that solving for the neutron transport equation's angular flux, ψ, is related to solving Eq. (1.1) for I. Additionally, we will assume that a steady-state, source-free, pure absorber neutron transport problem taxes DFEM schemes in a manner similar to the way DFEM schemes are tested in time-dependent thermal radiative transfer simulations, in particular Marshak wave type problems [20].

2.1   History of DFEM for Neutron Transport

The linear discontinuous finite element method (LDFEM) for discrete ordinates neutron transport is widely used and has been extensively studied[10, 6, 15, 3]. However, the DFEM technique is not limited to linear trial spaces. Reed et. al [22] used arbitrary order DFEM S_N neutron transport in TRIPLET but, due to data storage limitations at the time, only LDFEM was computationally practical. As a result of these historical computing limitations, the accuracy of LDFEM[12], and LDFEM possesing the thick diffusion limit [11], the majority of reported DFEM radiation transport literature has focused on the LDFEM approximation. Higher order DFEM methods have received periodic attention; some older examples include the work of Walters [28] and Hennart and del Valle [7, 8]. More recent investigations of higher order DFEM trial spaces include those of Warsa and Prinja [31] and Wang and Ragusa [30, 29]. The primary focus of the work in [7, 8, 31, 30, 29] was the convergence rate of arbitrary order DFEM schemes.

Negative angular flux solutions of the neutron transport equation obtained with LDFEM have been well documented in [6, 15, 3]. While these negativities do not affect the order of convergence and can be tolerated for certain applications [13], some nonlinear problems, particularly radiative transfer calculations, can diverge if the angular intensities are negative. As a result, several methods to eliminate or inhibit negative solutions have been developed and can be categorized into one of three categories: ad-hoc fix-ups [6], strictly non-negative solution representations [15], and matrix lumping [3]. The first two methods result in nonlinear systems of equations, while matrix lumping yields linear systems of equations. By definition, ad-hoc fix-ups and strictly non-negative solution representations yield non-negative outflows in 1-D, 2-D, and 3-D geometries, regardless of material properties. Mass matrix lumping (applied to LDFEM) yields strictly positive outflows only in 1-D geometries, though it does otherwise inhibit negativities [3].

Solution positivity of even degree unlumped DFEM methods for 1-D problems has been noted previously [28, 7, 8]. In comparing DFEM methods to nodal transport methods, Walters derived the quadratic DFEM scheme from the nodal transport equations using the Padé(2,3) approximation to the exponential term and noted that this approximation would result in a strictly positive outflow, regardless of cell optical thickness [28]. Hennart and del Valle then showed for slab geometry that all even P degree polynomial DFEM schemes approximate the cell outflow angular flux as a Padé($P, P + 1$) function, which is a strictly positive approximation of the exponential [7, 8]. The positivity of even degree unlumped DFEM for 1-D problems was also shown in [31].

2.2 Mass Matrix Lumping Techniques

In this Section, we examine the idea of mass matrix lumping and its ability to ensure positive angular flux solutions of the neutron transport equation for arbitrary degree DFEM trial spaces in non-scattering 1-D slab geometries. We consider traditional lumping (TL), that constructs a diagonal mass matrix by collapsing all off-diagonal entries onto the main diagonal [3], and quadrature-based self-lumping (SL) methods [21], that yield a diagonal mass matrix by numerically integrating the DFEM equations using the DFEM interpolatory points as quadrature points. Restricting ourselves to equally-spaced interpolation points, self-lumping numerical integration with the greatest degree of accuracy is achieved through the use of closed Newton-Cotes formulae [1]. However, Newton-Cotes formulas with a large number of integration points are known to be oscillatory and are of relatively low-order accuracy, integrating polynomials at most of degree equal to the number of integration points. By considering solution representations that employ quadrature points as the interpolatory points, for example Gauss-Legendre (hereafter Gauss) or Lobatto-Gauss-Legendre (hereafter Lobatto) quadrature points [1], we wish to find methods that are self-lumping with a significantly higher accuracy. We analyze the combinations of Lagrange interpolatory points and numerical integration strategies given in Table 2.1 for positivity of the angular flux solution, local truncation error order, and spatial convergence order as a function of trial space polynomial degree. We limit the consideration of exact numerical integration schemes to those with equally-spaced interpolatory points, due to the fact that exact integration with any particular set of interpolatory points will always yield the same DFEM solution.

It has long been noted that traditional lumping (TL) with equally-spaced interpolatory points for 1-D LDFEM is equivalent to using the trapezoidal quadrature

Table 2.1: Nomenclature of numerical schemes.

Interpolation Point Type	Integration Strategy	Method Short Hand Name
Equally-Spaced	Exact spatial integration, with collapsing of mass matrix entries to the main diagonal	TL
Equally-Spaced	Numerical integration via Newton-Cotes quadrature restricted to interpolation points	SL Newton-Cotes
Gauss Quadrature	Numerical integration via Gauss quadrature restricted to interpolation points	SL Gauss
Lobatto Quadrature	Numerical integration via Lobatto quadrature restricted to interpolation points	SL Lobatto
Equally-Spaced	Exact spatial integration	Exact DFEM

rule to approximately integrate the mass matrix [27] while exactly integrating the gradient operator. Since the trapezoidal rule is identical to the closed Newton-Cotes formula with two points, we hypothesize that, for finite elements of arbitrary order using equally-spaced interpolatory points, traditional lumping is equivalent to using a closed Newton-Cotes formula to compute the mass matrix while exactly integrating the gradient operator. We demonstrate the equivalence between traditional lumping and closed Newton-Cotes formulae in the computation of the mass matrix.

Self-lumping (SL) based on Newton-Cotes formulae differs from traditional lumping in that SL Newton-Cotes generally does not exactly integrate the gradient operator. Coincidentally, the gradient operator is exactly integrated for linear/quadratic trial spaces using a 2-point/3-point Newton-Cotes formula, respectively. However, for higher degree polynomial trial spaces, the corresponding Newton-Cotes formula does not exactly integrate the gradient operator.

Self-lumping based on either Gauss or Lobatto quadratures exactly integrates the gradient operator in 1-D slab geometry for all degree of polynomial trial spaces; thus, there is no need to distinguish between exact integration and quadrature integration of the gradient operator for the SL Gauss and SL Lobatto schemes.

2.3 Lumping Techniques for the 1-D S_N Neutron Transport Equation with Arbitrary Order DFEM

We now derive the weak form of the 1-D S_N neutron transport equations discretized with DFEM and define the different mass matrix lumping techniques.

2.3.1 Weak Form Derivation

Consider the 1-D slab geometry S_N neutron transport equation:

$$\mu_d \frac{d\psi_d}{dx} + \Sigma_t \psi_d = Q_d \,, \tag{2.1}$$

where ψ_d is the angular flux $[1/[cm^2 - sec - ster]]$ in the μ_d direction, μ_d is the d'th directional cosine relative to the x-axis, Σ_t is the total interaction cross section $[cm^{-1}]$, and Q_d is a total source (fixed+scattering+fission) angular source in the direction of μ_d $[1/[cm^3 - sec - ster]]$. In all that follows, we consider only non-scattering, non-fissioning media (pure absorbers), thus Q_d will only be non-trivial if a fixed source is present in the problem. The scalar flux, ϕ $[n/cm^2 - sec]$, is defined as

$$\phi(x) = 2\pi \int_{-1}^{1} \psi(x, \mu_d) \, d\mu_d \,. \tag{2.2}$$

For simplicity, we derive the DFEM equations for a single-cell domain, with $x \in [x_L, x_R]$. A known angular flux, $\psi_{in,d}$, is defined on the incoming face of the domain for all μ_d. For $\mu_d > 0$, $\psi_{in,d}$ is defined only at x_L and for $\mu_d < 0$, $\psi_{in,d}$ is defined

10

at x_R. We begin our derivation by first transforming the physical geometry to a reference element, $s \in [-1, 1]$. This affine transformation is such that:

$$x = \bar{x} + \frac{\Delta x}{2} s \,, \tag{2.3a}$$

$$dx = \frac{\Delta x}{2} ds \,, \tag{2.3b}$$

with $\bar{x} = \frac{x_L + x_R}{2}$, and $\Delta x = x_R - x_L$. We seek a numerical approximation to the true angular flux ψ_d using Lagrange polynomials of degree P:

$$\psi_d(s) \approx \widetilde{\psi}_d(s) = \sum_{j=1}^{N_P} \psi_{j,d} b_j(s) \,, \tag{2.4}$$

where the $\widetilde{\psi}_d(s)$ denotes the numerical approximation. The basis functions b_j are the canonical Lagrange polynomials with interpolatory points s_j,

$$b_j(s) = \prod_{\substack{k=1 \\ k \neq j}}^{N_P} \frac{s - s_k}{s_j - s_k} \,, \tag{2.5}$$

and $N_P = P + 1$. To determine the N_P unknown coefficients of Eq. (3.4), we follow a standard discontinuous Galerkin procedure, successively multiplying Eq. (3.1) by weight function b_i and integrating by parts, hence generating N_P moment equations $(1 \leq i \leq N_P)$. We assume that the cross sections are constant per cell. Inserting our solution representation $\widetilde{\psi}_d$, the i-th moment equation is given by:

$$\mu_d \left[b_i(1)\widetilde{\psi}_d(1) - b_i(-1)\widetilde{\psi}_d(-1) - \int_{-1}^{1} \widetilde{\psi}_d(s) \frac{db_i}{ds} \ ds \right] + \frac{\Delta x \Sigma_t}{2} \int_{-1}^{1} b_i(s)\widetilde{\psi}_d(s) \ ds$$

$$= \frac{\Delta x}{2} \int_{-1}^{1} b_i(s) Q_d(s) \ ds \,. \tag{2.6}$$

11

We now introduce the upwind approximation to define the angular flux at the cell edges. For $\mu_d > 0$ the angular flux at the cell interfaces is

$$\widetilde{\psi}_d(-1) = \psi_{in,d} \text{ and} \tag{2.7a}$$

$$\widetilde{\psi}_d(1) = \sum_{j=1}^{N_P} \psi_{j,d} b_j(1) . \tag{2.7b}$$

Similarly for $\mu_d < 0$:

$$\widetilde{\psi}_d(-1) = \sum_{j=1}^{N_P} \psi_{j,d} b_j(-1) \text{ and} \tag{2.8a}$$

$$\widetilde{\psi}_d(1) = \psi_{in,d} . \tag{2.8b}$$

In Eq. (2.7a) and Eq. (3.9), $\psi_{in,d}$ is either the known angular flux outflow from the upwind cell or a boundary condition. Inserting the definition of $\widetilde{\psi}_d(s)$, Eq. (3.7) becomes, for $\mu_d > 0$,

$$\mu_d \left[b_i(1) \left(\sum_{j=1}^{N_P} \psi_{j,d} b_j(1) \right) - b_i(-1)\psi_{in,d} - \int_{-1}^{1} \left(\sum_{j=1}^{N_P} \psi_{j,d} b_j(s) \right) \frac{db_i}{ds} \ ds \right] +$$

$$\frac{\Delta x \Sigma_t}{2} \int_{-1}^{1} b_i(s) \left(\sum_{j=1}^{N_P} \psi_{j,d} b_j(s) \right) \ ds = \frac{\Delta x}{2} \int_{-1}^{1} b_i(s) Q_d(s) \ ds , \tag{2.9}$$

and, for $\mu_d < 0$,

$$\mu_d \left[b_i(1)\psi_{in,d} - b_i(-1) \left(\sum_{j=1}^{N_P} \psi_{j,d} b_j(-1) \right) - \int_{-1}^{1} \left(\sum_{j=1}^{N_P} \psi_{j,d} b_j(s) \right) \frac{db_i}{ds} \ ds \right]$$

$$+ \frac{\Delta x \Sigma_t}{2} \int_{-1}^{1} b_i(s) \left(\sum_{j=1}^{N_P} \psi_{j,d} b_j(s) \right) \ ds = \frac{\Delta x}{2} \int_{-1}^{1} b_i(s) Q_d(s) ds . \tag{2.10}$$

Considering all of the N_P moment equations at once we can write both Eq. (3.10) and Eq. (3.11) in a single matrix form:

$$\left(\mu_d \mathbf{G} + \frac{\Sigma_t \Delta x}{2} \mathbf{M}\right) \vec{\psi}_d = \frac{\Delta x}{2} \vec{Q}_d + \mu_d \psi_{in,d} \vec{f}. \tag{2.11}$$

In Eq. (3.12) we have made use of the following definitions: the vector of unknowns is given by

$$\vec{\psi}_d = [\psi_{1,d} \ \cdots \ \psi_{N_P,d}]^T , \tag{2.12}$$

the mass matrix $\mathbf{M}$ is:

$$\mathbf{M}_{ij} = \int_{-1}^{1} b_i(s) b_j(s) \ ds , \tag{2.13}$$

the fixed source moment vector, $\vec{Q}_d$, is a column vector of length N_P:

$$\vec{Q}_{d,i} = \int_{-1}^{1} b_i(s) Q_d(s) \ ds , \tag{2.14}$$

and $\vec{f}$ is a column vector of length N_P:

$$\vec{f}_i = \begin{cases} b_i(-1) & \text{for } \mu_d > 0 \\ -b_i(1) & \text{for } \mu_d < 0 \end{cases} . \tag{2.15}$$

$\mathbf{G}$ is a $N_P \times N_P$ matrix which we refer to as the gradient operator. When $\mu_d > 0$, $\mathbf{G}$ is given by:

$$\mathbf{G}_{ij} = b_i(1) b_j(1) - \int_{-1}^{1} \frac{db_i}{ds} b_j(s) \ ds . \tag{2.16a}$$

For $\mu_d < 0$, $\mathbf{G}$ is:

$$\mathbf{G}_{ij} = -b_i(-1) b_j(-1) - \int_{-1}^{1} \frac{db_i}{ds} b_j(s) \ ds . \tag{2.16b}$$

When interpolatory points are not located at the cell interfaces (i.e., at $s = \pm 1$), it can be noted that

1. $\vec{f}$ has N_P non-zero entries and

2. $b_i(\pm 1)b_j(\pm 1) \neq 0$ for all $i, j = 1, \ldots, N_P$.

When a Lagrange interpolatory point exists on the cell edges, then $\vec{f}$ has only one non-zero entry and the product $b_i(\pm 1)b_j(\pm 1) \neq 0$ only when $i = j = N_P$ for $\mu_d > 0$ or when $i = j = 1$ for $\mu_d < 0$, as is the case when equally-spaced points or a Lobatto quadrature are used as interpolation points.

We evaluate the integrals of Eq. (3.16) and Eq. (2.16) using a numerical quadrature. A method exactly integrates a quantity when the quadrature rule used to evaluate the integral is accurate for polynomials of degree equal to or greater than the polynomial degree of the integrand. In general, the matrices are dense and their entries are computed as:

$$\mathbf{M}_{ij} \approx \sum_{q=1}^{N_q} w_q b_i(s_q) b_j(s_q) , \tag{2.17}$$

$$\mathbf{G}_{ij} \approx sg(\mu_d) b_i(sg(\mu_d)) b_j(sg(\mu_d)) - \sum_{q=1}^{N_q} w_q \frac{db_i}{ds}\bigg|_{s=s_q} b_j(s_q) , \tag{2.18}$$

where N_q is the number of quadrature points to be used, w_q are the weights associated with quadrature points s_q, and $sg(a)$ is the sign function defined as

$$sg(a) = \begin{cases} +1 & \text{if } a > 0 \\ -1 & \text{if } a < 0 \end{cases} . \tag{2.19}$$

14

2.3.2 Traditional Lumping

The traditional lumping (TL) scheme replaces $\mathbf{M}$ with $\widehat{\mathbf{M}}$, the latter being formed by collapsing row entries onto the main diagonal via the following formula [3]:

$$\widehat{\mathbf{M}}_{ij} = \begin{cases} \sum_{j=1}^{N_P} \mathbf{M}_{ij} & \text{for} \;\; i = j \\ 0 & \text{otherwise} \end{cases}. \tag{2.20}$$

2.3.3 Quadrature-Based Lumping

An alternative method of mass matrix lumping restricts the quadrature points to the interpolatory points where:

$$b_i(s_j) = \begin{cases} 1 & \text{if } s_i = s_j \\ 0 & \text{otherwise} \end{cases}, \;\; i = 1, \ldots, N_P, \tag{2.21}$$

and the quadrature integration of Eq. (2.17) reduces to:

$$\mathbf{M}_{ij} = \begin{cases} w_i & i = j \\ 0 & \text{otherwise} \end{cases}. \tag{2.22}$$

As mentioned previously, we refer to the implicit lumping of Eq. (2.22) as self-lumping (SL). Self-lumping is a method to automatically generate a diagonal mass matrix. We note that self-lumping does not imply that the quadrature formula inexactly integrates the mass matrix.

2.3.4 Source Moment Evaluation

Historically, when discussing lumping techniques, the focus has been on matrix lumping [3] and little attention was paid to lumping source terms. For instance,

consider a δ-shaped volumetric sources (i.e., equal to 0 everywhere except at one given point). In such a case, the evaluation of $\vec{Q}_d$ using quadrature-based self-lumping schemes is an open question. Obviously, quadrature-based schemes cannot evaluate Eq. (2.14) for δ-sources. To address this, we expand the source on a Legendre polynomial basis:

$$\widehat{S}_d(s) \;=\; \sum_{n=0}^{P} S_n P_n(s) \tag{2.23a}$$

$$\text{with } S_n \;=\; \frac{2n+1}{2} \int_{-1}^{1} Q_d(s) P_n(s) \; ds \,, \tag{2.23b}$$

and evaluate $\vec{Q}_d$ as follows

$$\vec{Q}_{d,i} = \int_{-1}^{1} b_i(s) \widehat{S}_d(s) \; ds \,. \tag{2.24}$$

Note that if the right-hand-side of Eq. (2.24) is exactly integrated, this is equivalent to exactly integrating Eq. (2.14).

2.4   Quadrature Point Selection

We now discuss the properties of different numerical quadratures as applied to the 1-D DFEM S_N neutron transport equations. We consider three different types of interpolatory points: equally-spaced, Gauss quadrature, and Lobatto quadrature. On the $[-1, 1]$ interval, the $N_P = P + 1$ equally spaced interpolation points for a degree P polynomial trial space are:

$$s_j = -1 + (j-1)\frac{2}{P}, \quad j = 1, \ldots, N_P \,. \tag{2.25}$$

Self-lumping using equally-spaced interpolation points requires numerical integration with closed Newton-Cotes quadrature formulae. The N_P weights, w_j, used for

Newton-Cotes numerical integration at the interpolation points do not follow a concise pattern, so we refer the reader to [1]. The Gauss quadrature points are the N_P roots of the Legendre polynomial, $P_{N_P}(s)$ [1]. The corresponding weights are:

$$w_j = \frac{2}{(1 - s_j^2)} \left[P'_{N_P}(s_j) \right]^2 .$$ (2.26)

Lobatto quadrature points have fixed endpoints, $s_1 = -1$, $s_{N_P} = 1$. The remaining $N_P - 2$ points are the roots of $P'_{N_P-1}(s)$ [1], with corresponding weights:

$$w_j = \begin{cases} \frac{2}{N_P(N_P-1)} & j = 1, \ j = N_P \\ \frac{2}{N_P(N_P-1)\left[P_{N_P-1}(s_j) \right]^2} & \text{otherwise} \end{cases} .$$ (2.27)

The highest polynomial degree a particular self-lumping quadrature formula exactly integrates is given in Table 2.2 for Newton-Cotes, in Table 2.3 for Gauss, and Table 2.4 for Lobatto quadratures. Also listed in Table 2.2 - Table 2.4 is the maximum polynomial degree of the integrands present in the gradient and mass matrices.

Table 2.2: Accuracy of self-lumping closed Newton-Cotes quadratures for DFEM trial spaces of polynomial degree P.

Polynomial Degree of $\widetilde{\psi}$	$N_P = P + 1$	Degree of **M** integrand	Degree of **G** integrand	Quadrature Accuracy
1	2	2	1	1
2	3	4	3	3
3	4	6	5	3
4	5	8	7	5
5	6	10	9	5
P	$P+1$	$2P$	$2P-1$	Odd $\widetilde{\psi}$: P Even $\widetilde{\psi}$: $P+1$

Table 2.3: Accuracy of self-lumping Gauss quadratures for DFEM trial spaces of polynomial degree P.

Polynomial Degree of $\widetilde{\psi}$	$N_P = P+1$	Degree of **M** integrand	Degree of **G** integrand	Quadrature Accuracy
1	2	2	1	3
2	3	4	3	5
3	4	6	5	7
4	5	8	7	9
5	6	10	9	11
P	$P+1$	$2P$	$2P-1$	$2P+1$

Table 2.4: Accuracy of self-lumping Lobatto quadratures for DFEM trial spaces of polynomial degree P.

Polynomial Degree of $\widetilde{\psi}$	$N_P = P+1$	Degree of **M** integrand	Degree of **G** integrand	Quadrature Accuracy
1	2	2	1	1
2	3	4	3	3
3	4	6	5	5
4	5	8	7	7
5	6	10	9	9
P	$P+1$	$2P$	$2P-1$	$2P-1$

Since the accuracy of an $N_P = P+1$ point Gauss quadrature integration exceeds the polynomial degree of the **M** and **G** integrands for a trial space of degree P, using the SL Gauss scheme will strictly yield the same numerical solution as any DFEM scheme that exactly integrates **M** and **G**. Thus, the SL Gauss scheme yields the same numerical solution as the Exact DFEM scheme.

For linear and quadratic trial spaces, self-lumping methods using either Lobatto or equally-spaced interpolation points will yield identical solutions. This is a direct result of the two- and three-point Lobatto quadrature formulae being identical to the two- and three-point closed Newton-Cotes quadratures. This equivalence does

not hold for higher degree polynomial trial spaces because the Lobatto quadrature points will no longer correspond to the equally-spaced quadrature points.

By definition, TL uses equally-spaced interpolation points and exactly integrates the gradient operator. For cell-wise constant cross sections, TL is equivalent to a numerical integration scheme that:

1. uses equally-spaced interpolation points,

2. integrates the gradient operator exactly, and

3. uses a Newton-Cotes quadrature restricted to the DFEM interpolation points to compute the mass matrix.

To prove the third point, consider the following. With traditional lumping, $\mathbf{M}_{ij}$ is exactly computed and then a row-sum operation is performed on the rows of $\mathbf{M}$; thus the entries of the diagonal mass matrix computed for TL are

$$\widehat{\mathbf{M}}_{ii} = \sum_{j=1}^{N_P} \int_{-1}^{1} b_i(s)b_j(s) \; ds = \int_{-1}^{1} b_i(s) \left[\sum_{j=1}^{N_P} b_j(s) \right] \; ds$$
$$= \int_{-1}^{1} ds \, b_i(s) \qquad \forall i = 1, \ldots, N_P \,, \qquad (2.28)$$

because $\sum_{j}^{N_P} b_j(s) = 1 \; \forall \; s \in [-1, +1]$ by definition. The integral $\int_{-1}^{1} ds \, b_i(s)$ is exactly integrated using a closed Newton-Cotes formula with $N_P = P + 1$ points since $b_i(s)$ is a polynomial of degree P. Finally, when the b_i functions are defined using equally-spaced points, the use of a closed Newton-Cotes formula with N_P points yields

$$\widehat{\mathbf{M}}_{ii} = \int_{-1}^{1} ds \, b_i(s) = \sum_{q=1}^{N_P} w_q b_i(s_q) = w_i \,, \qquad (2.29)$$

because $b_i(s_q) = \delta_{iq}$. Thus, the diagonal mass matrix computed using TL contains the closed Newton-Cotes weights as diagonal entries and is equivalent to approximating

19

M using closed Newton-Cotes quadrature in Eq. (2.22). We also numerically verify this in Table 2.5 for polynomial degrees up to 4. For linear and quadratic trial

Table 2.5: Equivalence of traditional lumping and closed Newton-Cotes quadrature approximation of the mass matrix.

P	Exact Integration of **M**	Row Sums of **M**	Newton-Cotes w with $P+1$ points
1	$\begin{bmatrix} \frac{2}{3} & \frac{1}{3} \\ \frac{1}{3} & \frac{2}{3} \end{bmatrix}$	$\begin{bmatrix} 1 \\ 1 \end{bmatrix}$	$\begin{bmatrix} 1 \\ 1 \end{bmatrix}$
2	$\begin{bmatrix} \frac{4}{15} & \frac{2}{15} & -\frac{1}{15} \\ \frac{2}{15} & \frac{16}{15} & \frac{1}{15} \\ -\frac{1}{15} & \frac{2}{15} & \frac{4}{15} \end{bmatrix}$	$\begin{bmatrix} \frac{1}{3} \\ \frac{4}{3} \\ \frac{1}{3} \end{bmatrix}$	$\begin{bmatrix} \frac{1}{3} \\ \frac{4}{3} \\ \frac{1}{3} \end{bmatrix}$
3	$\begin{bmatrix} \frac{16}{105} & \frac{38}{280} & -\frac{3}{70} & \frac{19}{840} \\ \frac{33}{280} & \frac{27}{35} & -\frac{27}{280} & -\frac{3}{70} \\ -\frac{3}{70} & -\frac{27}{280} & \frac{27}{35} & \frac{33}{280} \\ \frac{19}{840} & -\frac{3}{70} & \frac{38}{280} & \frac{16}{105} \end{bmatrix}$	$\begin{bmatrix} \frac{1}{4} \\ \frac{3}{4} \\ \frac{3}{4} \\ \frac{1}{4} \end{bmatrix}$	$\begin{bmatrix} \frac{1}{4} \\ \frac{3}{4} \\ \frac{3}{4} \\ \frac{1}{4} \end{bmatrix}$
4	$\begin{bmatrix} \frac{292}{2835} & \frac{296}{2835} & -\frac{58}{945} & \frac{8}{405} & -\frac{29}{2835} \\ \frac{296}{2835} & \frac{256}{405} & -\frac{128}{945} & \frac{256}{2835} & \frac{8}{405} \\ -\frac{58}{945} & -\frac{128}{945} & \frac{208}{315} & -\frac{128}{945} & -\frac{58}{945} \\ \frac{8}{405} & \frac{256}{2835} & -\frac{128}{945} & \frac{256}{405} & \frac{296}{2835} \\ -\frac{29}{2835} & \frac{8}{405} & -\frac{58}{945} & \frac{296}{2835} & \frac{292}{2835} \end{bmatrix}$	$\begin{bmatrix} \frac{7}{45} \\ \frac{32}{45} \\ \frac{4}{15} \\ \frac{32}{45} \\ \frac{7}{45} \end{bmatrix}$	$\begin{bmatrix} \frac{7}{45} \\ \frac{32}{45} \\ \frac{4}{15} \\ \frac{32}{45} \\ \frac{7}{45} \end{bmatrix}$

spaces, the 2-point and 3-point Newton-Cotes quadrature formulae exactly integrate the gradient operator, as shown in Table 2.2. Thus, for linear and quadratic trial spaces, schemes that use

1. equally-spaced interpolation points and traditional lumping,

2. equally-spaced interpolation points and self-lumping numerical integration, or

3. Lobatto quadrature interpolation points and self-lumping numerical integration,

will yield identical solutions.

2.5 Numerical Results

In this Section, we present numerical results for two 1-D slab problems. For the first problem, we consider a source-free pure absorber with vacuum boundary conditions on the right, a known angular flux $\psi_{in,d}$ incident on the left face, and a spatially constant total cross section Σ_t. The second problem consists of a slab with vacuum boundary conditions on both sides, no scattering, constant Σ_t, and a fixed δ-source.

For $\mu_d > 0$, the numerical approximations to the angular flux near the cell inflow and outflow are as follows:

$$\widetilde{\psi}_{in,d} = \sum_{j=1}^{N_P} \psi_{j,d} b_j(-1) \text{ and} \tag{2.30}$$

$$\widetilde{\psi}_{out,d} = \sum_{j=1}^{N_P} \psi_{j,d} b_j(1) . \tag{2.31}$$

Regardless of the sign of μ_d, the numerical approximation to the cell average angular flux is defined as:

$$\widetilde{\psi}_{A,d} = \frac{1}{2} \sum_{j=1}^{N_P} w_j \psi_{j,d} . \tag{2.32}$$

We used the following quadrature weight normalization: $\sum_{j=1}^{N_P} w_j = 2$. In Eq. (2.30), Eq. (2.31), and Eq. (2.32), $\psi_{j,d}$ are the components of $\vec{\psi}_d$, the numerical solution obtained by solving Eq. (3.12). Hence, the numerical angular flux solution of any of the previously discussed DFEM schemes can be obtained as a function of h, the number of mean free paths divided by μ_d,

$$h = \frac{\Sigma_t \Delta x}{\mu_d} . \tag{2.33}$$

2.5.1 Incident Flux Single-Cell Outflow Comparison

For the incident-flux problem, the analytical solution of Eq. (3.1) is:

$$\psi(x, \mu_d) = \begin{cases} \psi_{in,d} \exp\left[-\frac{\Sigma_t(x-x_L)}{\mu_d}\right] & \text{for } \mu_d > 0 \\ 0 & \text{for } \mu_d < 0 \end{cases} . \tag{2.34}$$

The analytic angular flux outflow, $\psi_{out,d} = \psi(x_R, \mu_d)$, is:

$$\psi_{out,d} = \psi_{in,d} \exp[-h] . \tag{2.35}$$

Similarly, the analytic average angular flux within the cell, $\psi_{A,d}$, is:

$$\psi_{A,d} = \frac{1}{\Delta x} \int_{x_L}^{x_R} \psi(x, \mu_d) \, dx = \frac{\psi_{in,d}}{h} \left(1 - \exp[-h]\right) . \tag{2.36}$$

The solution components are given by

$$\vec{\psi}_d = \psi_{in,d} \left(\mathbf{G} + \frac{h}{2}\mathbf{M}\right)^{-1} \vec{f}, \tag{2.37}$$

which allows us to compare the various choices of interpolatory points and numerical integration strategies solely as a function of h.

Figures 2.1-2.4 show the numerically calculated cell outflow, $\widetilde{\psi}_{out,d}$, as a function of h for all methods considered. All methods converge to the analytical solution as $h \to 0$, thus we have zoomed in the range where the methods visually differ (i.e., $h \geq 1$). We observe that:

- SL Gauss yields strictly positive outflows for even degree polynomial trial spaces,
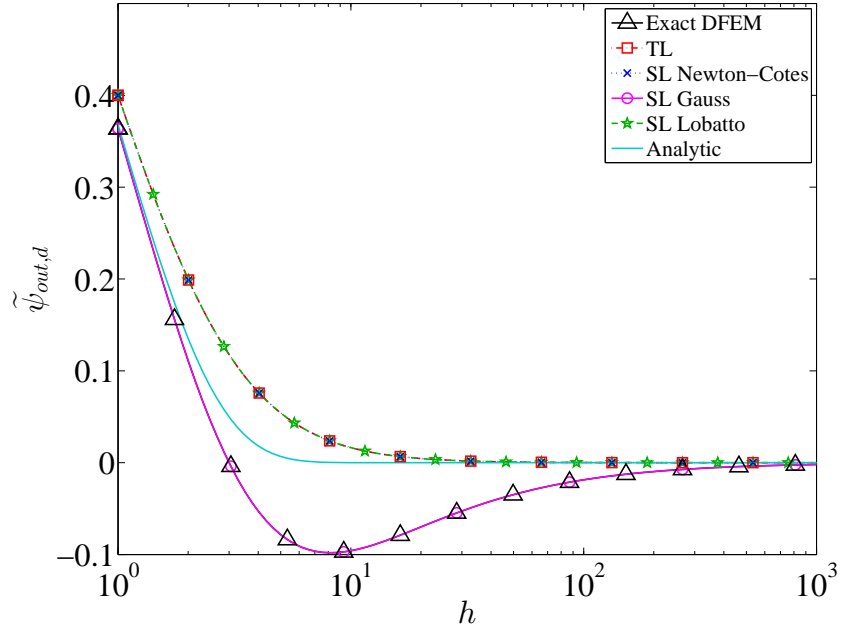
Figure 2.1: Numerical outflow values as a function of h, for a single cell homogeneous absorber problem with a linear DFEM trial space.
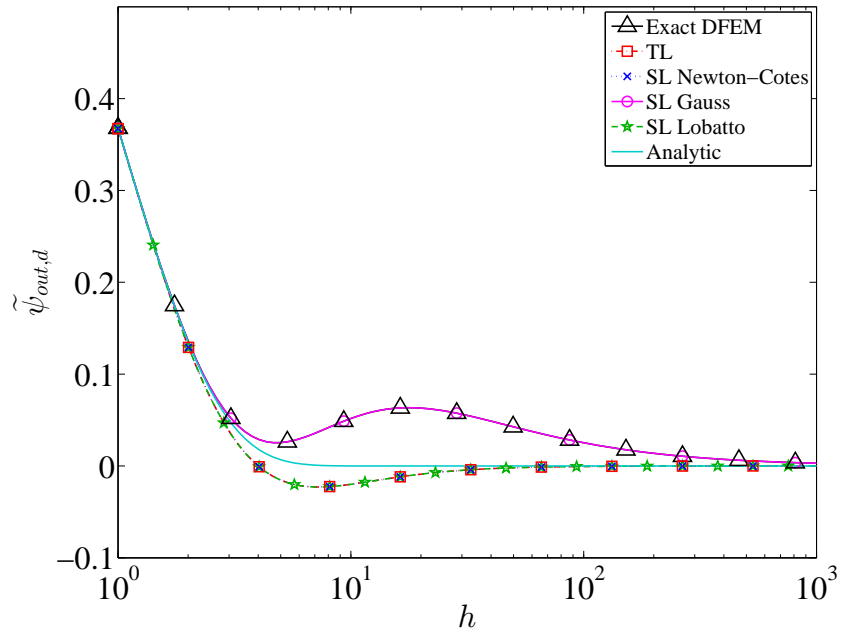
Figure 2.2: Numerical outflow values as a function of h, for a single cell homogeneous absorber problem with a quadratic DFEM trial space.
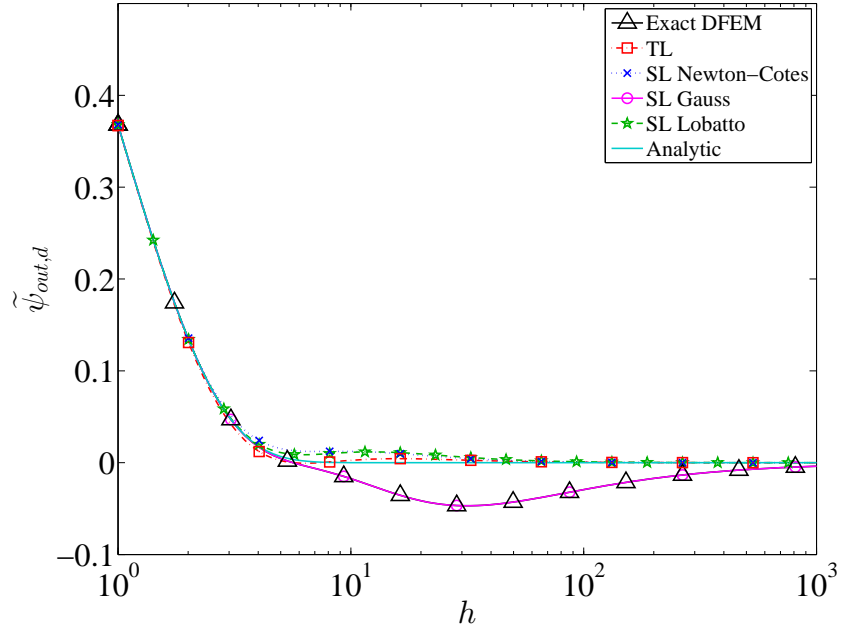
Figure 2.3: Numerical outflow values as a function of h, for a single cell homogeneous absorber problem with a cubic DFEM trial space.
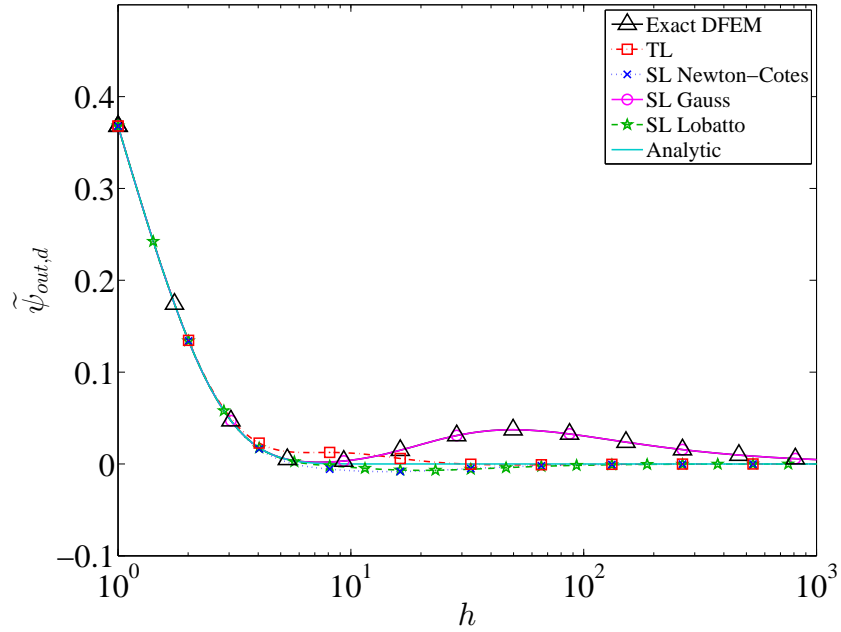
Figure 2.4: Numerical outflow values as a function of h, for a single cell homogeneous absorber problem with a quartic DFEM trial space.

- SL Lobatto and SL Newton-Cotes yield strictly positive outflows for odd degree polynomial trial spaces, and

- TL yields strictly positive outflows only for a linear trial space.

We also numerically verify the remarks made of Section 2.4, that is:

- SL Gauss is equivalent to Exact DFEM,

- SL Lobatto, SL Newton-Cotes, and TL are equivalent for linear and quadratic trial spaces, and

- for even degree trial spaces, the outflow value computed by SL Gauss is not monotonically decreasing as a function of h for cells of intermediate optical thickness (the same was noted in [31] for Exact DFEM).

2.5.2   Fixed Source Single-Cell Inflow Comparison

As noted in [15], it is possible for LDFEM to yield negative solutions near cell inflows for source driven problems. In this second problem, we use a δ-source:

$$Q_d(x) = \begin{cases} \delta(x - x_o) & \text{for} \ \ \mu_d > 0 \\ 0 & \text{for} \ \ \mu_d < 0 \end{cases}, \tag{2.38}$$

$x \in [-1, 1]$, and $-1 \leq x_o \leq 1$. The analytic solution to this problem for $\mu_d > 0$ is:

$$\psi(x, \mu_d) = \begin{cases} \exp\left[-\frac{\Sigma_t(x-x_o)}{\mu_d}\right] & x \geq x_o \\ 0 & x < x_o \end{cases}. \tag{2.39}$$

(For $\mu_d < 0$, $\psi(x, \mu_d) = 0$.) We now examine the numerical approximation to the angular flux near the cell inflow, $\widetilde{\psi}_{in,d}$, for various integration schemes, trial space degrees, and as a function of the ratio of the first Legendre moment of the source, S_1,

25

to the zero-th Legendre moment of the source, S_0. Note that the physical range of that ratio, $\frac{S_1}{S_0}$, is $[-3, 3]$, corresponding to a δ-source at the left cell edge ($\frac{S_1}{S_0} = -3$) or at the right edge ($\frac{S_1}{S_0} = 3$).

We first consider the case of a vacuum ($\Sigma_t = 0$), thus only testing the effect of quadrature accuracy in evaluating $\vec{Q}_d$ and $\mathbf{G}$. In Figs. 2.5-2.8, we plot $\widetilde{\psi}_{in,d}$ for three schemes:

1. Lobatto quadrature, which is exact for $\mathbf{G}$ and approximate for the source moments, Eq. (2.24) ,

2. Gauss quadrature: which is exact for both $\mathbf{G}$ and the source moments, and

3. Newton-Cotes quadrature: which is approximate for both $\mathbf{G}$ and the source moments.

Figure 2.5: Numerical inflow values as a function of $\frac{S_1}{S_0}$ for a single cell (vacuum case) with a δ-shaped source, using linear DFEM.

Figure 2.6: Numerical inflow values as a function of $\frac{S_1}{S_0}$ for a single cell (vacuum case) with a δ-shaped source, using quadratic DFEM.

The dotted vertical lines in Figs. 2.5-2.8 correspond to the extrema values of $\frac{S_1}{S_0}$ that yield a strictly positive polynomial source representation of degree P (indeed, the degree-P Legendre expansion of the δ-source is not everywhere positive for a wide range of possible $\frac{S_1}{S_0}$ that are physically realizable). For all trial space degrees, the Gauss scheme exhibits less negativity than either of the other two schemes. The dramatic difference between the Gauss scheme and the Lobatto scheme is solely due to the quadrature formula used to evaluate $\vec{Q}_d$ since both schemes exactly integrate $\mathbf{G}$. The Newton-Cotes scheme exhibits less severe negativities than the Lobatto scheme but is less robust than the Gauss scheme. Given the results shown in Figs. 2.5-2.8, we conclude that the most robust schemes exactly integrate the source moments, Eq. (2.24).
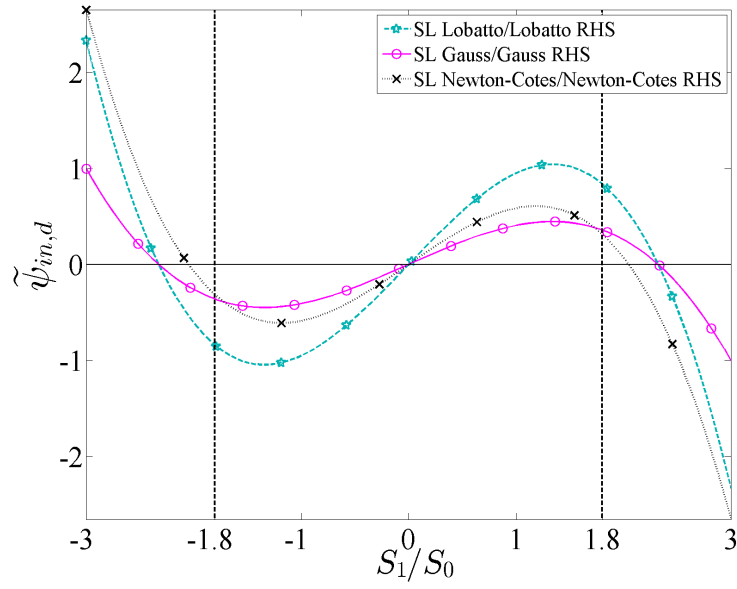
Figure 2.7: Numerical inflow values as a function of $\frac{S_1}{S_0}$ for a single cell (vacuum case) with a δ-shaped source, using cubic DFEM.
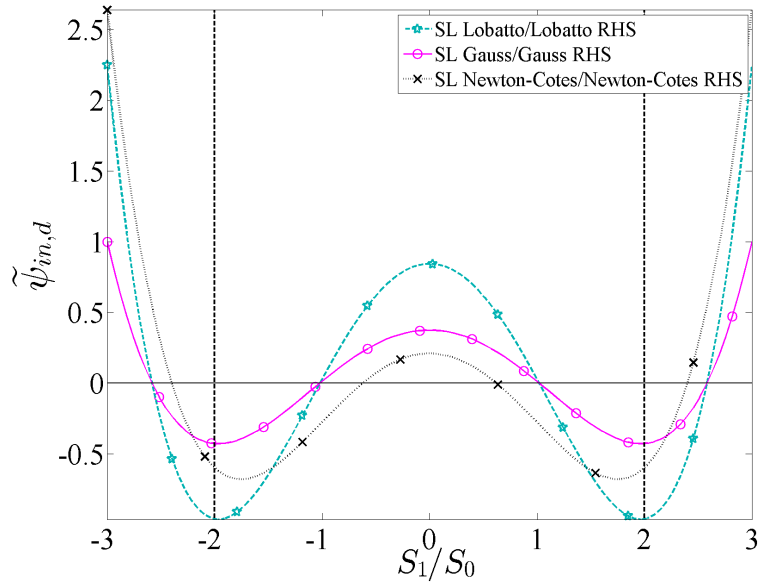
Figure 2.8: Numerical inflow values as a function of $\frac{S_1}{S_0}$ for a single cell (vacuum case) with a δ-shaped source, using quartic DFEM.
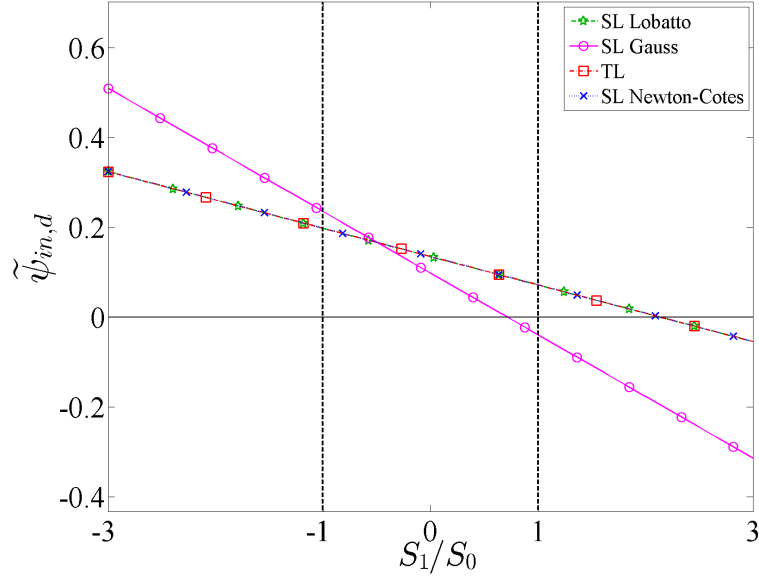
Figure 2.9: Numerical inflow values as a function of $\frac{S_1}{S_0}$, for a single cell (absorber case) with a δ-shaped source, using linear DFEM.
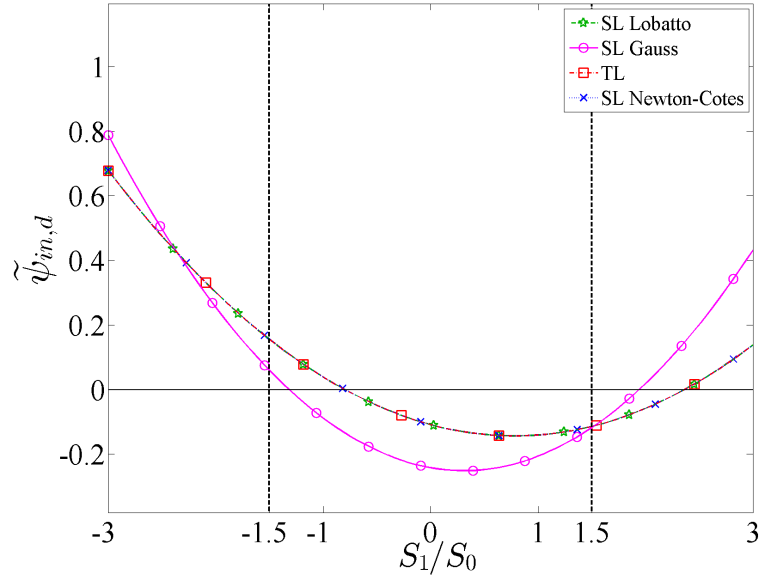
Figure 2.10: Numerical inflow values as a function of $\frac{S_1}{S_0}$, for a single cell (absorber case) with a δ-shaped source, using quadratic DFEM.
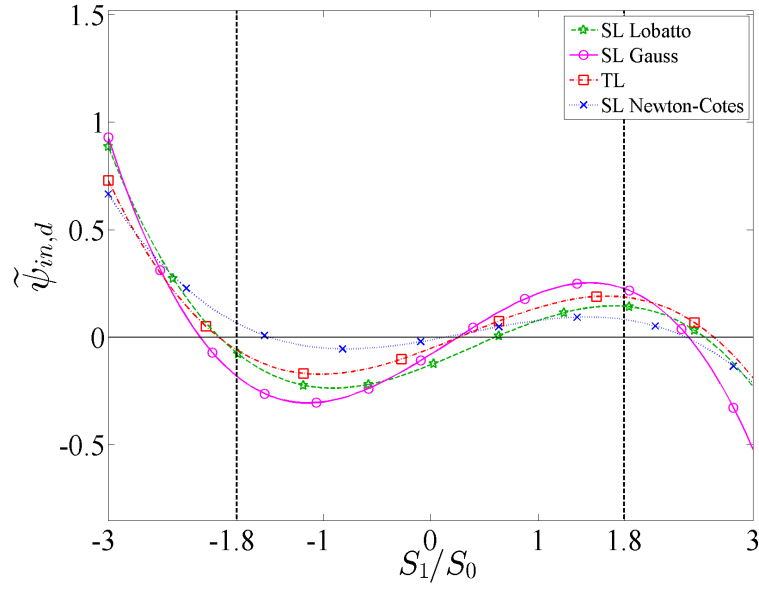
Figure 2.11: Numerical inflow values as a function of $\frac{S_1}{S_0}$, for a single cell (absorber case) with a δ-shaped source, using cubic DFEM.

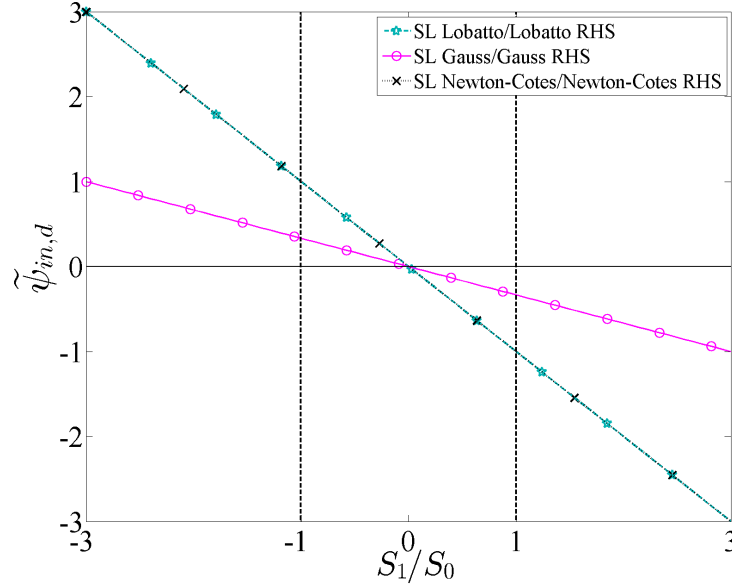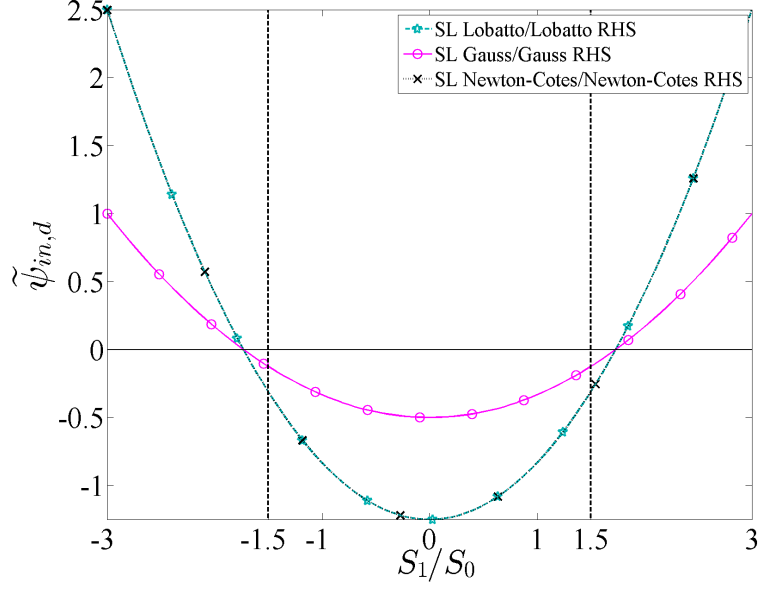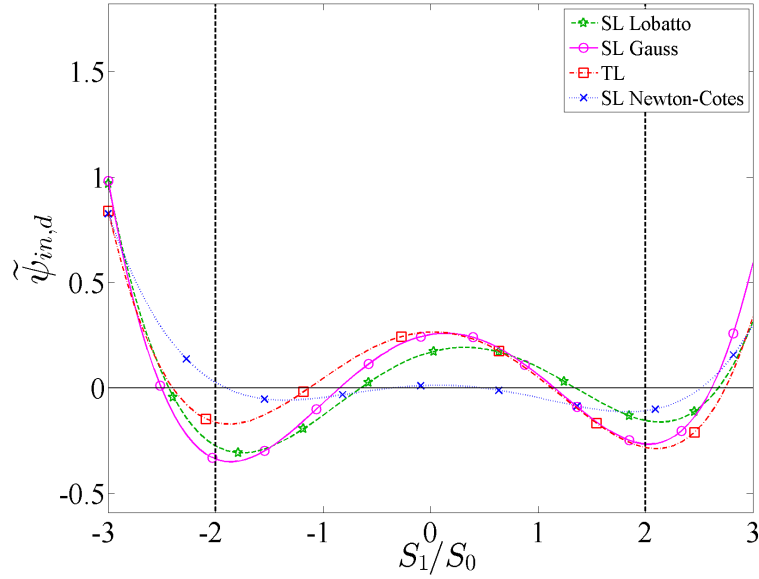Figure 2.12: Numerical inflow values as a function of $\frac{S_1}{S_0}$, for a single cell (absorber case) with a δ-shaped source, using quartic DFEM.

In Figs. 2.9-2.12, we again examine the positivity of $\widetilde{\psi}_{in,d}$, but for a non-vacuum case. Total cell optical thickness was chosen to be 5 mean free paths in Figs. 2.9-2.12 because this value led to the clearest plots. The relative behaviors observed do not change with cell optical thickness, but using a thicker domain reduces the magnitude for the values of $\widetilde{\psi}_{in,d}$. All methods in Figs. 2.9-2.12 exactly integrate Eq. (2.24). Regardless of trial space chosen, all schemes exhibit some negativities, but the SL Gauss scheme exhibits the greatest negativities and oscillations. The SL Newton-Cotes scheme presents the least severe negativities.

2.5.3 Single-Cell Taylor Series Analysis

Next, we perform a local truncation error analysis by comparing the Taylor series expansions for the exact and numerical angular fluxes as a function of powers of h for the source-free, incident flux pure absorber problem. Matlab [17] has been employed to perform the symbolic Taylor series expansions about $h = 0$. We denote the Taylor-expanded quantities using the subscript T. The expansions for the analytical inflow, cell average, and outflow are given below:

$$\psi_{in,d,T} = \psi_{in,d} \tag{2.40a}$$

$$\psi_{A,d,T} = \psi_{in,d}\left(1 - \frac{h}{2} + \frac{h^2}{6} - \frac{h^3}{24} + \frac{h^4}{120} - \frac{h^5}{720}\dots\right) \tag{2.40b}$$

$$\psi_{out,d,T} = \psi_{in,d}\left(1 - h + \frac{h^2}{2} - \frac{h^3}{6} + \frac{h^4}{24} - \frac{h^5}{120}\dots\right). \tag{2.40c}$$

The Taylor expansions of the numerical analogues to the quantities in Eqs. (2.40) depend on the trial space polynomial degree, the choice of interpolatory points, and the numerical integration strategy. For brevity, we omit giving these numerical analogues. Table 2.6 gives the lowest order term for the difference between $\psi_{in,d,T}$ and the numerical analogs for the Exact DFEM and TL schemes. The same information

for the SL Newton-Cotes, SL Gauss, and SL Lobatto schemes is given in Table 2.7. The differences between $\psi_{A,d,T}$ and the respective numerical analogs are given in Table 2.8 for Exact DFEM and TL, and Table 2.9 for the SL Newton-Cotes, SL Gauss, and SL Lobatto schemes. Differences between ψ{out}, d, T and the correseponding numerical analogs are given in Table 2.10 for Exact DFEM and TL and Table 2.11 gives the lowest order difference between the SL Newton-Cotes, SL Gauss, and SL Lobatto approximations of $\psi_{out,d,T}$. In Tables 2.6-2.11 all entries are listed as $q(C)$, to be read as "the difference between the analytic taylor expansion and the numeric analog is Ch^q with $h = \Sigma_t \Delta x / \mu$". Entries of "Machine Precision" in Tables 2.6-2.11 are meant to indicate that the difference between the analytic Taylor expansion and Taylor expansion of the numerical approximation was inconclusive due to all coefficients being within machine precision.

Table 2.6: Local truncation error analysis in $\widetilde{\psi}_{in,d}$ for a single cell problem with constant cross section, for Exact DFEM and TL.

Polynomial Degree of $\widetilde{\psi}$	Exact DFEM	TL
1	2 (2×10^{-1})	2 (5×10^{-1})
2	3 (2×10^{-2})	3 (4×10^{-2})
3	4 (1×10^{-3})	2 (7×10^{-2})
4	5 (7×10^{-5})	3 (1×10^{-2})
5	6 (3×10^{-6})	2 (5×10^{-2})
6	7 (1×10^{-7})	3 (1×10^{-2})
7	8 (4×10^{-9})	2 (5×10^{-2})

Table 2.7: Local truncation error analysis in $\widetilde{\psi}_{in,d}$ for a single cell problem with constant cross section, for SL Newton-Cotes, SL Gauss, and SL Lobatto.

Polynomial Degree of $\widetilde{\psi}$	SL Newton-Cotes	SL Gauss	SL Lobatto
1	2 (5×10^{-1})	2 (2×10^{-1})	2 (5×10^{-1})
2	3 (4×10^{-2})	3 (2×10^{-2})	3 (4×10^{-2})
3	2 (1×10^{-1})	4 (1×10^{-3})	4 (3×10^{-3})
4	3 (1×10^{-2})	5 (7×10^{-5})	5 (1×10^{-4})
5	2 (6×10^{-2})	6 (3×10^{-6})	6 (7×10^{-6})
6	3 (9×10^{-3})	7 (1×10^{-7})	7 (3×10^{-7})
7	2 (4×10^{-2})	8 (4×10^{-9})	8 (8×10^{-9})

Table 2.8: Local truncation error analysis in $\widetilde{\psi}_{A,d}$ for a single cell problem with constant cross section, for Exact DFEM and TL.

Polynomial Degree of $\widetilde{\psi}$	Exact DFEM	TL
1	3 (1×10^{-2})	2 (2×10^{-1})
2	5 (1×10^{-4})	4 (2×10^{-3})
3	7 (7×10^{-7})	3 (3×10^{-3})
4	9 (2×10^{-9})	5 (8×10^{-5})
5	11 (5×10^{-12})	3 (1×10^{-3})
6	13 (7×10^{-15})	5 (7×10^{-5})
7	Machine Precision	3 (1×10^{-3})

Table 2.9: Local truncation error analysis in $\widetilde{\psi}_{A,d}$ for a single cell problem with constant cross section, for SL Newton-Cotes, SL Gauss, and SL Lobatto

Polynomial Degree of $\widetilde{\psi}$	SL Newton-Cotes	SL Gauss	SL Lobatto
1	2 (2×10^{-1})	3 (1×10^{-2})	2 (2×10^{-1})
2	4 (2×10^{-3})	5 (1×10^{-4})	4 (2×10^{-3})
3	4 (6×10^{-4})	7 (7×10^{-7})	6 (1×10^{-5})
4	6 (8×10^{-6})	9 (2×10^{-9})	8 (5×10^{-8})
5	6 (2×10^{-6})	11 (5×10^{-12})	10 (1×10^{-10})
6	8 (2×10^{-8})	13 (7×10^{-15})	12 (2×10^{-13})
7	8 (3×10^{-9})	Machine Precision	Machine Precision

Table 2.10: Local truncation error analysis in $\widetilde{\psi}_{out,d}$ for a single cell with constant cross section, for Exact DFEM and TL.

Polynomial Degree of $\widetilde{\psi}$	Exact DFEM	TL
1	4 (1×10^{-2})	3 (2×10^{-1})
2	6 (1×10^{-4})	5 (2×10^{-3})
3	8 (7×10^{-7})	4 (3×10^{-3})
4	10 (2×10^{-9})	6 (1×10^{-2})
5	12 (5×10^{-12})	4 (1×10^{-3})
6	14 (7×10^{-15})	6 (7×10^{-5})
7	Machine Precision	4 (1×10^{-3})

Table 2.11: Local truncation error analysis in $\widetilde{\psi}_{out,d}$ for a single cell with constant cross section, for SL Newton-Cotes, SL Gauss, and SL Lobatto.

Polynomial Degree of $\widetilde{\psi}$	SL Newton-Cotes	SL Gauss	SL Lobatto
1	3 (2×10^{-1})	4 (1×10^{-2})	3 (2×10^{-1})
2	5 (2×10^{-3})	6 (1×10^{-4})	5 (2×10^{-3})
3	5 (6×10^{-4})	8 (7×10^{-7})	7 (1×10^{-5})
4	7 (8×10^{-6})	10 (2×10^{-9})	9 (5×10^{-8})
5	7 (2×10^{-6})	12 (5×10^{-12})	11 (1×10^{-10})
6	9 (2×10^{-8})	14 (7×10^{-15})	13 (2×10^{-13})
7	9 (3×10^{-9})	Machine Precision	Machine Precision

This local truncation error analysis illustrates the following.

1. Exact DFEM and SL Gauss, which are equivalent, exactly integrate the mass matrix, and are the most accurate,

2. TL does not guarantee increasing order of accuracy by using higher degree polynomial trial spaces,

3. TL converges at most third or fifth order for $\widetilde{\psi}_{A,d}$ and fourth or sixth order for $\widetilde{\psi}_{out,d}$ for odd or even polynomial trial spaces, respectively,

4. SL Newton-Cotes increases in accuracy with higher degree polynomial trial spaces, but only for $\widetilde{\psi}_{out,d}$ and $\widetilde{\psi}_{A,d}$,

5. TL and SL Newton-Cotes are at most second order or third order accurate for $\widetilde{\psi}_{in,d}$ for odd or even polynomial trial spaces, respectively,

6. SL Gauss is order $2P+1$ accurate in calculating $\widetilde{\psi}_{A,d}$ and order $2P+2$ accurate in calculating $\widetilde{\psi}_{out,d}$,

7. SL Lobatto is order $2P$ accurate in calculating $\widetilde{\psi}_{A,d}$ and order $2P+1$ in calculating $\widetilde{\psi}_{out,d}$,

8. SL Gauss, SL Lobatto, and Exact DFEM are accurate to order $P+1$ in calculating $\widetilde{\psi}_{in,d}$, and

9. SL Gauss is more accurate than SL Lobatto (smaller error constant) in computing $\widetilde{\psi}_{in,d}$, but not an order of h .

2.5.4 Convergence Rates for Spatially Discretized 1-D Domains

Here, we consider a homogeneous pure absorber material placed in a 1-D slab configuration and uniformly mesh the domain using N_{cells} cells. We use: $x \in [0, 10 \ cm]$, $\Sigma_t = 1 \ [cm^{-1}]$, no external sources, vacuum conditions on the right face of the slab, and a normally incident unit beam on the left face. The analytical solution to this problem is trivial to obtain:

$$\psi(x, \mu_d) = \begin{cases} \exp\left[-\Sigma_t x\right] & \mu_d = 1 \\ 0 & \text{otherwise} \end{cases} . \tag{2.41}$$

35

The L_2 norm of the error is:

$$E_\psi = \sqrt{\sum_{i=1}^{N_{cells}} \int_{x_{i-1/2}}^{x_{i+1/2}} \left(\psi(x,\mu_d) - \widetilde{\psi}_{d,i}(x) \right)^2 \, dx} \,, \tag{2.42}$$

where we recall that $\widetilde{\psi}_{d,i}(x)$ is the DFEM approximation of the angular flux in cell i. To evaluate the above integral, we use a high-order Gauss quadrature set $(x_{f,q}, \, w_{f,q})$ that employs a large number of quadrature points:

$$E_\psi \approx \sqrt{\sum_{i=1}^{N_{cells}} \frac{\Delta x_i}{2} \sum_{q=1}^{N_{qf}} w_{f,q} \left(\psi(x_{f,q},\mu_d) - \widetilde{\psi}_d(x_{f,q}) \right)^2} \,. \tag{2.43}$$

Values of E_ψ shown here are calculated using $N_{qf} = 10$. In addition to the L_2 error, we also present the cell average angular flux error, E_{ψ_A}, defined as

$$E_{\psi_A} = \sqrt{\sum_{i=1}^{N_{cells}} \Delta x_i \left(\psi_{A,d,i} - \widetilde{\psi}_{A,d,i} \right)^2} \,, \tag{2.44}$$

and the cell outflow error, $E_{\psi_{out}}$, given by:

$$E_{\psi_{out}} = \sqrt{\sum_{i=1}^{N_{cells}} \Delta x_i \left(\psi(x_{i+1/2},\mu_d) - \widetilde{\psi}_{out,d,i} \right)^2} \,. \tag{2.45}$$

In Eq. (2.43), Eq. (2.44), and Eq. (2.45), Δx_i is the cell width of cell i and $\psi_{A,d,i}$ is the exact cell-averaged angular flux in cell i, which, for $\mu_d = 1$, is simply:

$$\psi_{A,d,i} = \exp[-\Sigma_t x_{i-1/2}] \frac{1}{\Delta x_i} \left(1 - \exp[-\Sigma_t \Delta x_i] \right) \,. \tag{2.46}$$

In the plots that follow, we omit plotting the errors of Exact DFEM since the Exact DFEM solution is identical to that of SL Gauss. For linear and quadratic polynomi-

als, we plot only SL Lobatto and omit plotting TL and SL Newton-Cotes since these methods yield identical solutions for linear and quadratic trial spaces.   Figures
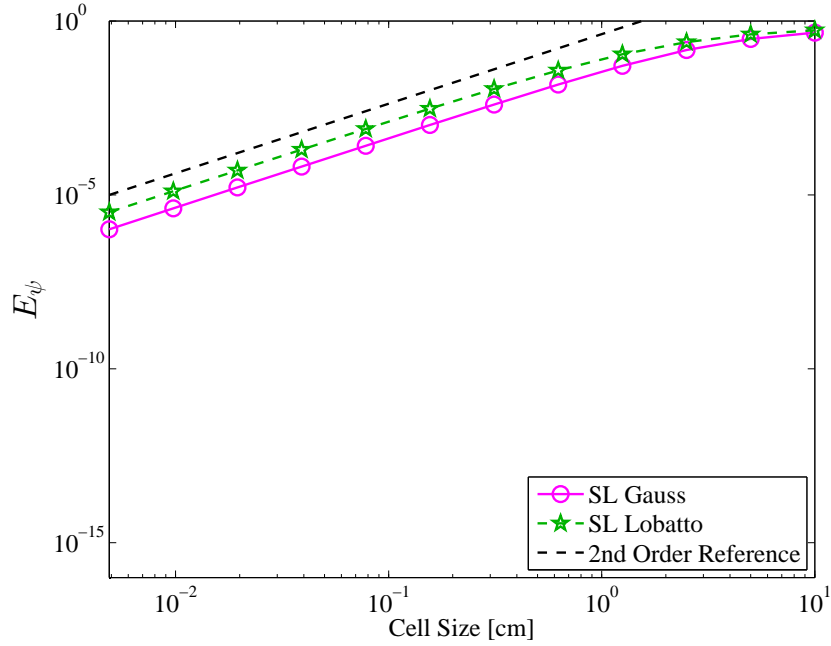
Figure 2.13: Convergence rate of the L_2 norm of the error, E_ψ, as a function of the mesh cell size for a pure absorber discretized with linear DFEM.

2.13-2.16 mirror the results of Table 2.6 and Table 2.7, which is expected since the convergence rate of E_ψ will be limited by the slowest converging local approximation which is $\widetilde{\psi}_{in,d}$. Similarly, Figs. 2.17-2.20 are the multiple-cell analogue of the local truncation error analysis of $\widetilde{\psi}_{A,d}$ given in Table 2.8 and Table 2.9. $E_{\psi_{out}}$, as shown in Figs. 2.21-2.24, does not converge at the local truncation error rates of Table 2.10 and Table 2.11.
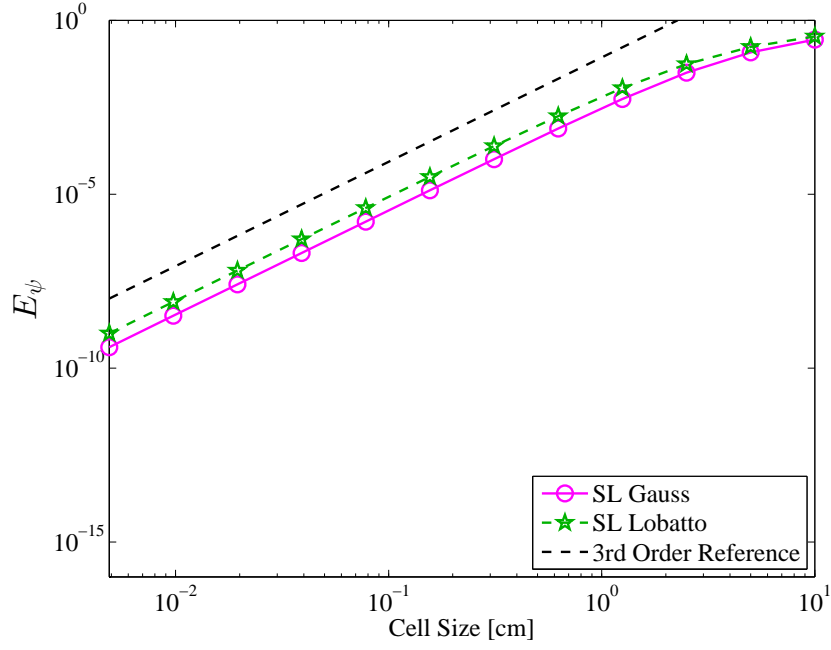
Figure 2.14: Convergence rate of the L_2 norm of the error, E_ψ, as a function of the mesh cell size for a pure absorber discretized with quadratic DFEM.
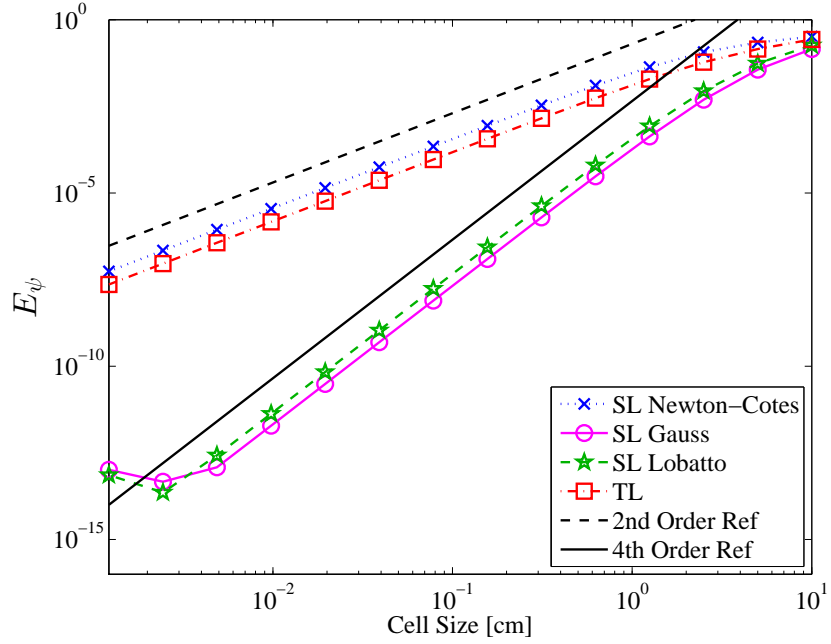
Figure 2.15: Convergence rate of the L_2 norm of the error, E_ψ, as a function of the mesh cell size for a pure absorber discretized with cubic DFEM.
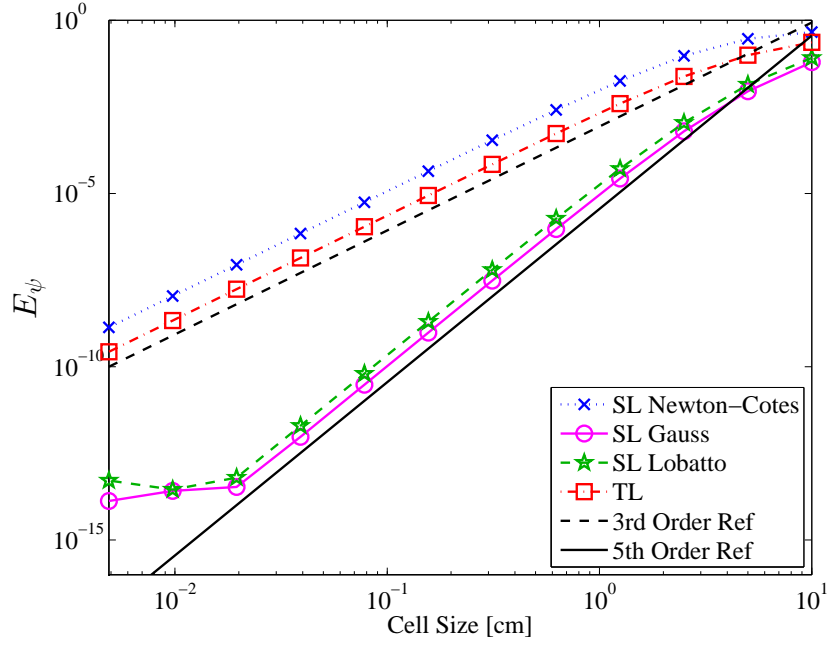
Figure 2.16: Convergence rate of the L_2 norm of the error, E_ψ, as a function of the mesh cell size for a pure absorber discretized with quartic DFEM.
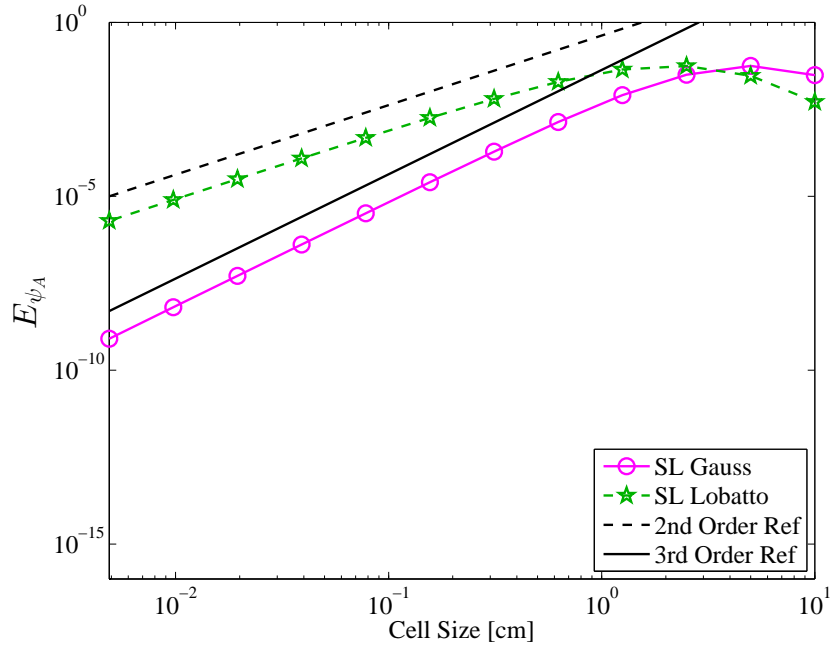
Figure 2.17: Convergence rate for $E_{\psi,A}$ as a function of the mesh cell size for a homogeneous pure absorber and linear DFEM.
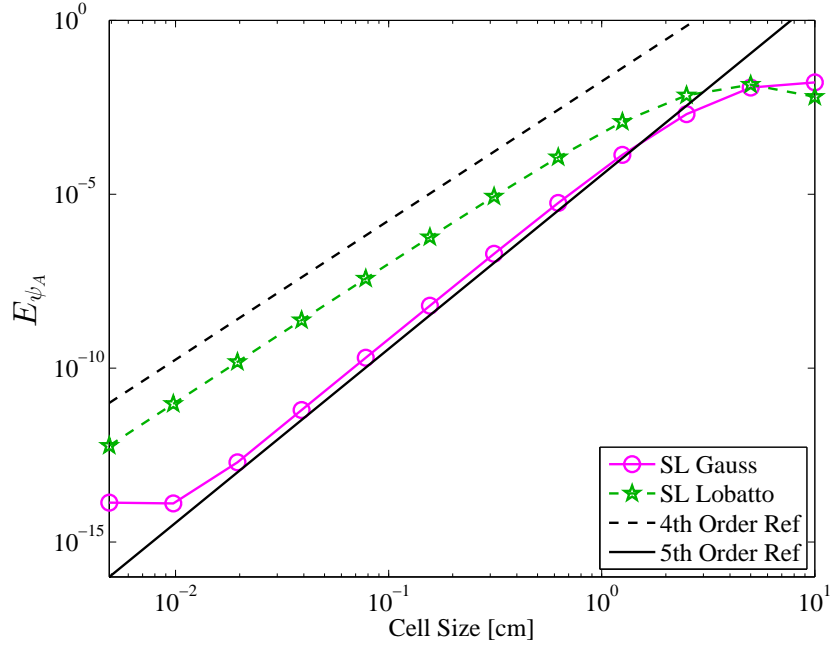
Figure 2.18: Convergence rate for $E_{\psi,A}$ as a function of the mesh cell size for a homogeneous pure absorber and quadratic DFEM.
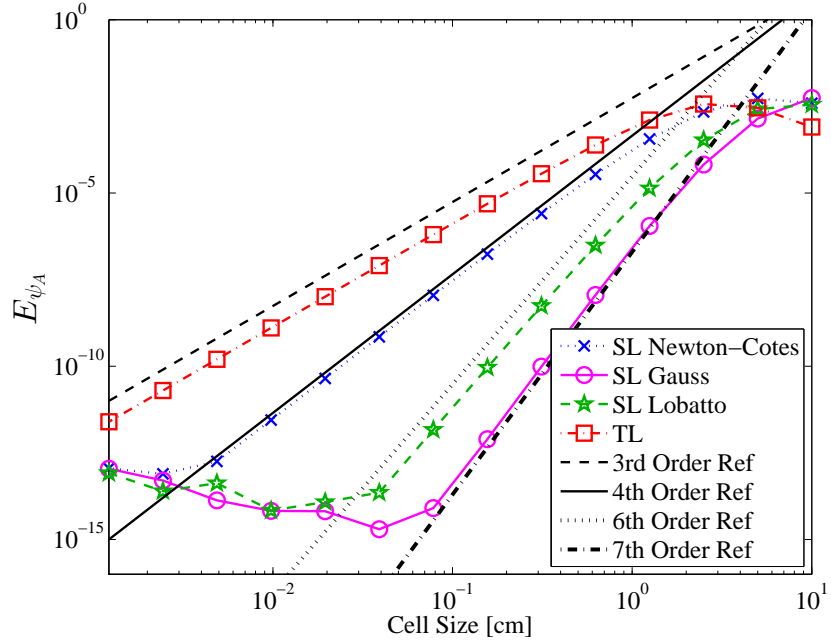
Figure 2.19: Convergence rate for $E_{\psi,A}$ as a function of the mesh cell size for a homogeneous pure absorber and cubic DFEM.
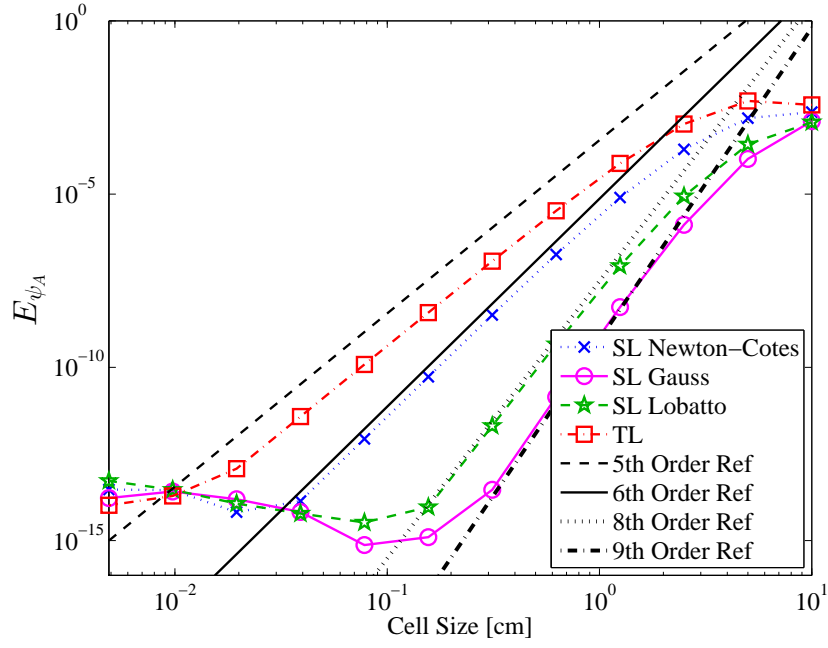
Figure 2.20: Convergence rate for $E_{\psi,A}$ as a function of the mesh cell size for a homogeneous pure absorber and quartic DFEM.
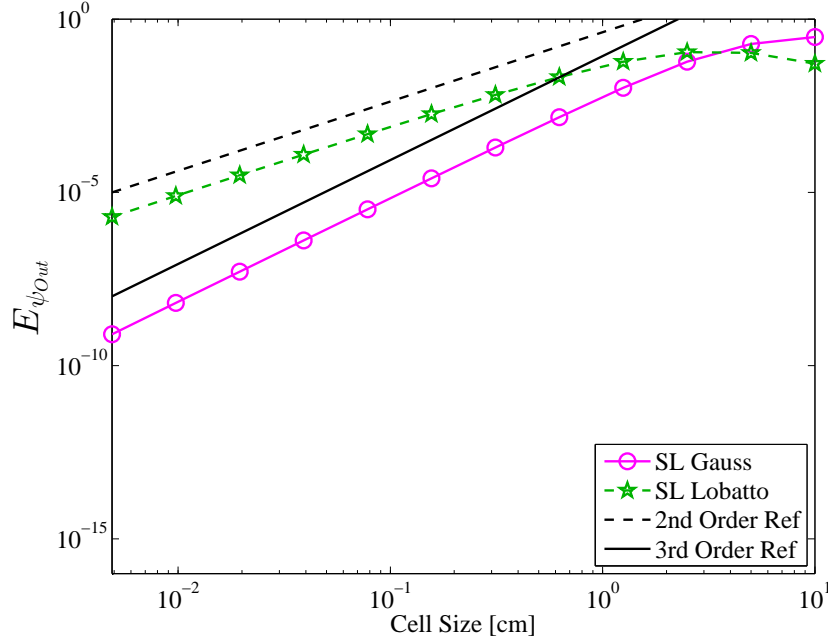
Figure 2.21: Convergence rate of $E_{\psi,out}$ as a function of the mesh cell size for a homogeneous pure absorber for linear DFEM.
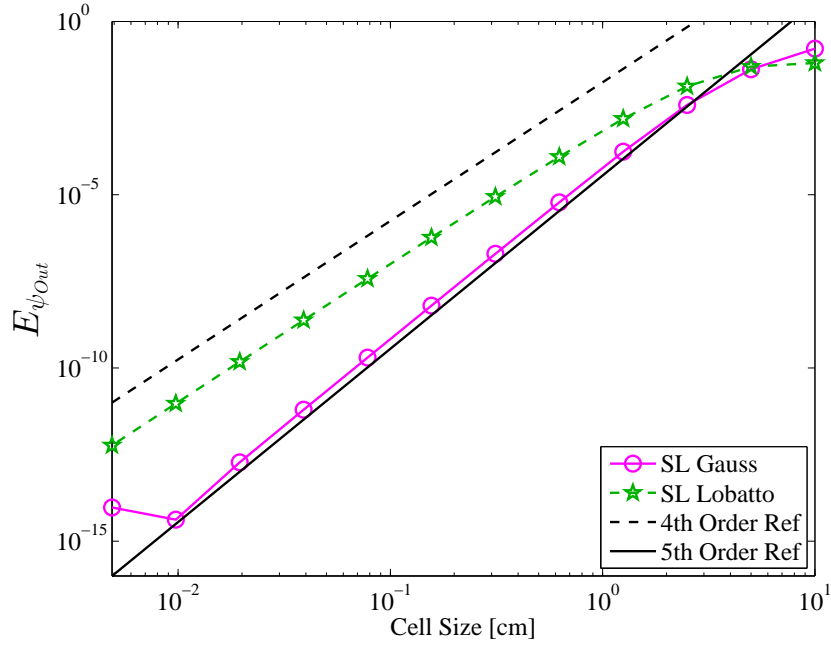
Figure 2.22: Convergence rate of $E_{\psi,out}$ as a function of the mesh cell size for a homogeneous pure absorber for quadratic DFEM.
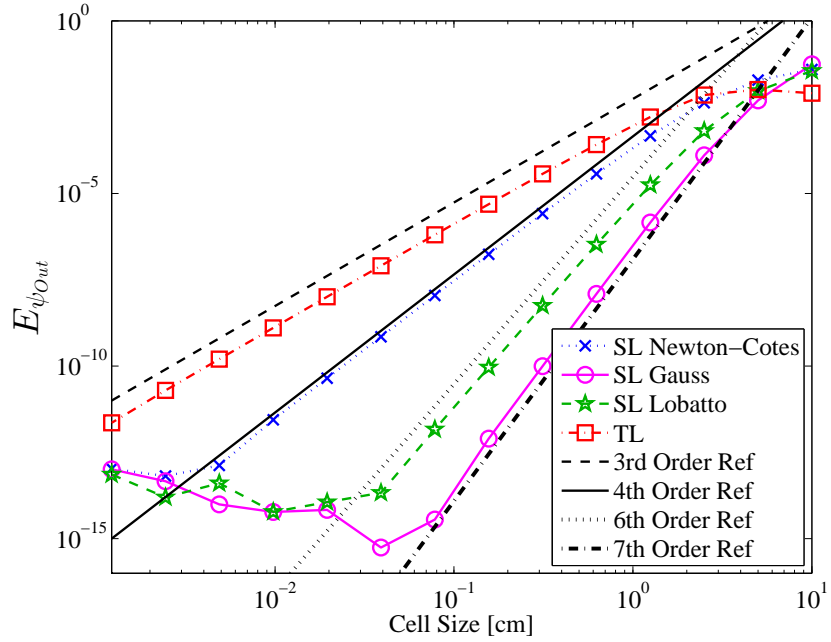
Figure 2.23: Convergence rate of $E_{\psi,out}$ as a function of the mesh cell size for a homogeneous pure absorber for cubic DFEM.
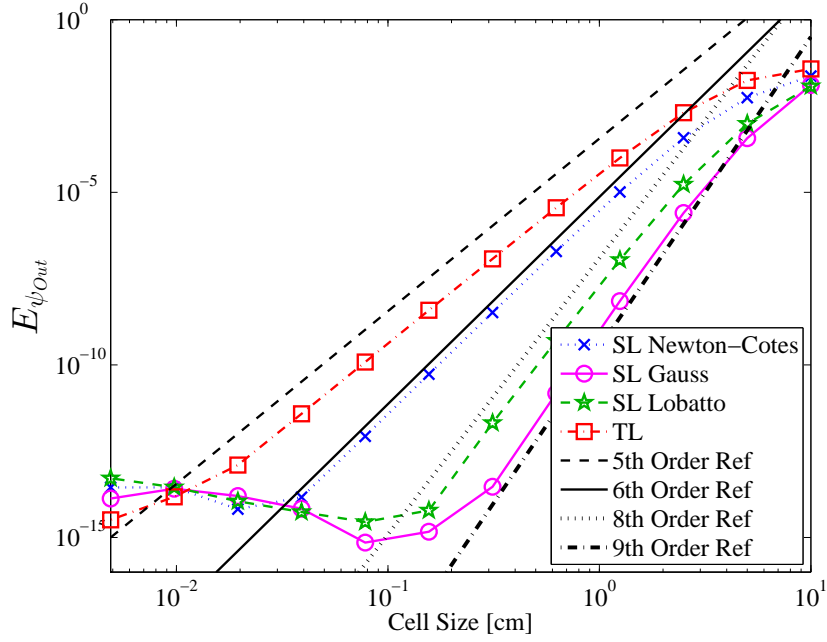
Figure 2.24: Convergence rate of $E_{\psi,out}$ as a function of the mesh cell size for a pure absorber for quartic DFEM.

The accumulation of errors in multiple-cell problems causes $E_{\psi_{out}}$ to globally converge one order of accuracy lower than the local truncation orders given in Table 2.10 and Table 2.11. It should be noted that the plateauing of errors E_{ψ}, E_{ψ_A}, and $E_{\psi_{out}}$ to values $\approx 10^{-14}$ in Figs. 2.13-2.16, Figs. 2.17-2.20, and Figs. 2.21-2.24, respectively, is simply a result of our numerical solutions being limited by machine precision (double precision).

3.   LAST CHAPTER: THE IMPORTANCE OF RESEARCH

Thermal radiative transfer interaction opacities can be rapidly varying functions of temperature. For example, consider Marshak wave problems and the canonical T^{-3} dependence [20] of absorption opacity. Opacity variations of several orders of magnitude near the heated/cold material interface are easily possible. Historically, the neutron transport and thermal radiative transfer communities assumed interaction cross section and opacities, respectively, were cell-wise constant [3, 14, 18]. Adams first described [2] and then presented computational results [4] for a "simple" corner balance (SCB) spatial discretization method that explicitly accounted for the spatial variation of opacity within individual spatial cells. The SCB scheme (which can be shown to be related to a LDFEM for certain geometries) accounts for opacity spatial variation within each cell via vertex-based quadrature evaluation. Similar strategies have been adapted to LDFEM radiative diffusion [20] and LDFEM TRT [19] calculations. For accurate TRT solutions, use of higher order DFEM will requires the development of corresponding higher order strategies for treating the within cell spatial variation of opacities.

For many problems of interest to the nuclear science and engineering community, macroscopic cross sections in neutronics and opacities in radiative transfer calculations cannot accurately be described as piecewise constants in space. Cross sections and opacities are functions of continuously varying quantities such as temperature, density, burn-up history, etc. [25]. Examples of simulations that may not be adequately described by cell-wise constant cross sections include nuclear reactor depletion calculations and radiative transfer calculations for high energy density physics experiments. However, the majority of neutron transport literature has only con-

sidered the case of cell-wise constant cross sections, see [3, 14, 32, **?**]. The work of Kavenoky and Lautard [9] and more recently Santandrea and Bellier [24] are notable exceptions in neutronics. In [9], continuous cubic finite element diffusion calculations that assume a linearly varying spatial cross section within each mesh cell were compared to results obtained using the same spatial discretization but with the assumption that cross sections are constant in each cell. Similarly, [24] compared the results of a linear characteristic scheme that assumes a linearly varying cross section in each spatial cell to those of a linear characteristic scheme that assumes a constant cross section in each cell. Spatial variation of opacity within individual mesh cells for radiative transfer calculations was first proposed by Adams in [2] for "simple" corner balance (SCB) spatial discretization methods and the first SCB computational results for a problem with spatially varying cross section in each cell appeared in [4]. The practice of accounting for spatially varying cross sections has become become standard in the radiative transfer community for linear spatial discretizations, usually implemented via a vertex-based quadrature evaluation of mass matrix terms (for a finite element discretization), as in [20] and [19], or through corner balance schemes as originally outlined by Adams.

In this work, we analyze the effects of cross-section spatial dependence on solution accuracy. Our work differs from [9]-[4] by considering a discontinuous finite element (DFEM) spatial discretization of the slab geometry S_N transport equation using arbitrary degree polynomial finite element trial spaces. In addition, like [2] and [4] we do not make any approximation to the particular spatial shape of the cross-section spatial variation in each cell. We build on the quadrature integration ideas presented in [16] and employ a numerical quadrature to evaluate the mass matrix integrals that involve cross sections as a function of space. In general, the quadrature integration of the DFEM interaction term with arbitrary spatial cross section form will not

be exact. However, we showed in Section 2 that exact computation of integrals appearing in the DFEM weak form, when cross sections are spatially constant, is not required to achieve high-order accuracy with high-order DFEM approximations. Building on this idea, we investigate the effects of using numerical quadratures to compute DFEM mass matrices, accounting for the spatial variation of cross section in space. As in Section 2 we use self-lumping numerical quadratures [21, 27], restricting quadrature integration points to the DFEM polynomial interpolation points. Results are compared as a function of DFEM polynomial trial space degree and interpolation point type.

We demonstrate that assuming a piecewise constant cross section in each cell, when the cross section is not cell-wise constant in space, has several undesirable effects. Considering a source-free, purely absorbing medium, we show that DFEM schemes that assume a cell-wise constant cross section are at most second-order accurate for the angular flux solution and limited to at most first-order accuracy for the interaction rate solution, regardless of the DFEM polynomial trial space degree. We also show that assuming a piecewise constant cross section results in a highly discontinuous, non-monotonic spatial interaction rate. This phenomena has likely been present in published numerical results for problems with non-piecewise constant cross section but was not observed previously due to the choice of data presentation.

We then consider schemes that explicitly account for cross-section spatial variation within individual mesh cells. First, the positivity and robustness of different schemes are discussed using a source-free pure absorber problem. Next, we demonstrate that self-lumping schemes that evaluate the DFEM weak form integrals involving cross section with quadrature result in fully accurate schemes for arbitrary degree polynomial DFEM. By fully accurate we mean schemes that achieve the same

46

order of convergence for problems with spatially varying and cell-wise constant cross section, for a given DFEM approximation order

3.1   Weak Form Derivation

We begin by considering the 1-D slab geometry S_N transport equation:

$$\mu_d \frac{d\psi_d(x)}{dx} + \Sigma_t(x)\psi_d(x) = Q_d(x) \,. \tag{3.1}$$

In Eq. (3.1), $\psi_d(x)$ is the angular flux $[1/[cm^2 - sec - ster]]$ in μ_d, the directional cosine relative to the x-axis, $\Sigma_t(x)$ is the total interaction cross section $[cm^{-1}]$, and $Q_d(x)$ is the total angular source in the direction of μ_d $[1/[cm^3 - sec - ster]]$. Q_d includes both scattering and fixed sources. The scalar flux, $\phi(x)$ is defined as:

$$\phi(x) = 2\pi \int_{-1}^{1} \psi(x,\mu) \; d\mu \approx 2\pi \sum_d w_d \psi_d(x) \,. \tag{3.2}$$

We derive the DFEM equations for a single cell, $x \in [x_L, x_R]$, with extension to multiple cells being straightforward. A known angular flux, $\psi_{in,d}$, is defined on the incoming face of each cell for a given direction μ_d. $\psi_{in,d}$ comes either from a known boundary condition or from the cell outflow of the upwind cell. We first transform from the physical geometry to a reference element, $s \in [-1, 1]$, such that:

$$x = \frac{x_L + x_R}{2} + \frac{\Delta x}{2}s \tag{3.3a}$$

$$dx = \frac{\Delta x}{2}ds \,, \tag{3.3b}$$

with $\Delta x = x_R - x_L$. The true angular flux solution, $\psi_d(x)$, is approximated by a Lagrange interpolatory polynomial, $\widetilde{\psi}_d(x)$, of degree P:

$$\psi_d(s) \approx \widetilde{\psi}_d(s) = \sum_{j=1}^{N_P} \psi_{j,d} b_j(s) \,. \tag{3.4}$$

The b_j's are the Lagrange interpolatory functions with interpolatory points s_j,

$$b_j(s) = \prod_{\substack{k=1 \\ k \neq j}}^{N_P} \frac{s - s_k}{s_j - s_k} \,, \tag{3.5}$$

and $N_P = P + 1$. We stress that the interpolatory points, s_j, are not necessarily equally-spaced points. The total angular source, $Q(s, \mu)$, is expanded in a similar fashion:

$$Q_d(s) \approx \widetilde{Q}_d(s) = \sum_{j=1}^{N_P} Q_d(s_j) b_j(s) \,. \tag{3.6}$$

To determine the N_P unknowns of Eq. (3.4), we follow the standard Galerkin procedure, successively multiplying Eq. (3.1) by weight function b_i and integrating the result by parts, hence generating N_P moment equations. Inserting our solution representation $\widetilde{\psi}_d$, the i-th, exact moment equation is:

$$\mu_d \left[b_i(1)\widetilde{\psi}_d(1) - b_i(-1)\widetilde{\psi}_d(-1) - \int_{-1}^{1} \widetilde{\psi}_d(s)\frac{db_i}{ds}\ ds \right] + \frac{\Delta x}{2} \int_{-1}^{1} \Sigma_t(s)b_i(s)\widetilde{\psi}_d(s)\ ds$$

$$= \frac{\Delta x}{2} \int_{-1}^{1} b_i(s)\widetilde{Q}_d(s)\ ds \,. \tag{3.7}$$

48

We use the upwind approximation to define the angular flux at the cell edges. For $\mu_d > 0$ the angular flux at the cell interfaces is

$$
\begin{aligned}
\widetilde{\psi}_d(-1) &= \psi_{in,d} & \text{(3.8a)} \\
\widetilde{\psi}_d(1) &= \sum_{j=1}^{N_P} \psi_{j,d} b_j(1)\,. & \text{(3.8b)}
\end{aligned}
$$

Similarly for $\mu_d < 0$:

$$
\begin{aligned}
\widetilde{\psi}_d(-1) &= \sum_{j=1}^{N_P} \psi_{j,d} b_j(-1) & \text{(3.9a)} \\
\widetilde{\psi}_d(1) &= \psi_{in,d}\,. & \text{(3.9b)}
\end{aligned}
$$

In Eqs. (3.8)-(3.9), $\psi_{in,d}$ is a known angular flux outflow from either the upwind cell or boundary conditions. Using definition of Eqs. (3.8), Eq. (3.7) becomes, for $\mu_d > 0$,

$$
\mu_d \left[b_i(1) \left[\sum_{j=1}^{N_P} \psi_{j,d} b_j(1) \right] - b_i(-1)\psi_{in,d} - \int_{-1}^{1} \left[\sum_{j=1}^{N_P} \psi_{j,d} b_j(s) \right] \frac{db_i}{ds}\, ds \right] +
$$

$$
\frac{\Delta x}{2} \int_{-1}^{1} \Sigma_t(s) b_i(s) \left[\sum_{j=1}^{N_P} \psi_{j,d} b_j(s) \right]\, ds = \frac{\Delta x}{2} \int_{-1}^{1} b_i(s) \left[\sum_{j=1}^{N_P} Q_d(s_j) b_j(s) \right]\, ds\,. \quad \text{(3.10)}
$$

For $\mu_d < 0$, using the definition of Eqs. (3.9) yields:

$$
\mu_d \left[b_i(1)\psi_{in,d} - b_i(-1) \left[\sum_{j=1}^{N_P} \psi_{j,d} b_j(-1) \right] - \int_{-1}^{1} \left[\sum_{j=1}^{N_P} \psi_{j,d} b_j(s) \right] \frac{db_i}{ds}\, ds \right]
$$

$$
+ \frac{\Delta x}{2} \int_{-1}^{1} \Sigma_t(s) b_i(s) \left[\sum_{j=1}^{N_P} \psi_{j,d} b_j(s) \right]\, ds = \frac{\Delta x}{2} \int_{-1}^{1} b_i(s) \left[\sum_{j=1}^{N_P} Q_d(s_j) b_j(s) \right]\, ds\,.
$$

$$
\text{(3.11)}
$$

Considering all N_P moment equations simultaneously, we write both Eq. (3.10) and Eq. (3.11) as:

$$\mu_d \mathbf{L} \vec{\psi}_d - \mu_d \psi_{in,d} \vec{f} + \frac{\Delta x}{2} \mathbf{R}_{\Sigma_t} \vec{\psi}_d = \frac{\Delta x}{2} \mathbf{M} \vec{Q}_d \,. \tag{3.12}$$

In Eq. (3.12) we use the following definitions for the vector of unknowns, $\psi_{j,d}$, and total source components, $Q_{j,d}$:

$$\vec{\psi}_d = [\psi_{1,d} \ \dots \ \psi_{N_P,d}]^T \tag{3.13}$$

$$\vec{Q}_d = [Q_d(s_1) \ \dots \ Q_d(s_{N_P})]^T \,. \tag{3.14}$$

We define the $N_P \times N_P$ reaction matrix, $\mathbf{R}_{\Sigma_t}$, as:

$$\mathbf{R}_{\Sigma_t, ij} = \int_{-1}^{1} \Sigma_t(s) b_i(s) b_j(s) \ ds \,, \tag{3.15}$$

and the $N_P \times N_P$ mass matrix, $\mathbf{M}$, as:

$$\mathbf{M}_{ij} = \int_{-1}^{1} b_i(s) b_j(s) \ ds \,. \tag{3.16}$$

$\vec{f}$ is a length N_P column vector. For $\mu_d > 0$:

$$\vec{f}_i = b_i(-1) \,. \tag{3.17}$$

For $\mu_d < 0$:

$$\vec{f}_i = -b_i(1) \,. \tag{3.18}$$

50

$\mathbf{L}$ is a $N_P \times N_P$ matrix that we refer to as the gradient operator. When $\mu_d > 0$: $\mathbf{L}$ is:

$$\mathbf{L}_{ij} = b_i(1)b_j(1) - \int_{-1}^{1} \frac{db_i}{ds}b_j \ ds \,. \tag{3.19}$$

For $\mu_d < 0$, $\mathbf{L}$ is:

$$\mathbf{L}_{ij} = -b_i(-1)b_j(-1) - \int_{-1}^{1} \frac{db_i}{ds}b_j \ ds \,. \tag{3.20}$$

3.2   Numerical Schemes

We consider two classes of numerical methods in this paper. The first class uses exact spatial integration to evaluate the integrals that define $\mathbf{R}_{\Sigma_t}$, $\mathbf{M}$, and $\mathbf{L}$. A second class of methods uses numerical quadrature. Specifically, we limit out discussion of quadrature-based integration to so called self-lumping methods [16]. Self-lumping methods, first discussed in [21, 27] for parabolic problems, use numerical quadrature restricted to the finite element interpolation points, and thus naturally yield diagonal mass matrices. Earlier work for problems with cell-wise constant cross sections [16] demonstrated that, for S_N transport discretized with DFEM, robust and accurate methods can be developed using self-lumping techniques.

A shorthand notation is given in Table 2.1 for all of the numerical methods considered in this paper and described in detail in the remainder of this section.

3.2.1   Exact Spatial Integration

By exact spatial integration, we mean schemes that compute the entries of $\mathbf{M}$ and $\mathbf{L}$ exactly. Here, we achieve this by using equally-spaced interpolation points and employing a Gauss-Legendre quadrature rule [1] that exactly integrates the respective integrands. Two schemes use exact spatial integration. One approximates the spatially varying cross section as a cell-wise constant cross section. The other uses the exact cross section when integrating the weak form DFEM quantities involving

cross section. The scheme that assumes a cell-wise constant cross section represents the state of the practice in the neutron transport community, while the second scheme represents the ideal scenario for DFEM transport schemes in problems with spatially varying cross sections.

3.2.1.1 Exact Cross Section

The exact cross section, exact spatial integration scheme (EXS DFEM) analytically integrates $\mathbf{R}_{\Sigma_t}$. Note that since $\Sigma_t(x)$ can be an arbitrary function, analytic integration of $\mathbf{R}_{\Sigma_t}$ is in general impossible. Likewise, quadrature integration is unlikely to be exact. In our testing of the EXS DFEM scheme, we use a 20-point Gauss-Legendre quadrature to approximately integrate Eq. (3.15). Alternatively, adaptive quadrature, with a controllable tolerance, may be used such that the quadrature error in evaluating Eq. (3.15) could be reduced below some small tolerance.

3.2.1.2 Constant Cross Section

Historically, neutronics and some radiative transfer calculations have approximated spatially varying cross sections by assuming cell-wise constant cross sections [3, 14, 32, 18]. That is, some evaluation of the true $\Sigma_t(s)$ within a given cell is used to determine a constant value, $\hat{\Sigma}_t$, within each cell. Under this simplification, $\mathbf{R}_{\Sigma_t}$ is approximated as:

$$\mathbf{R}_{\Sigma_t} = \hat{\Sigma}_t \mathbf{M}. \tag{3.21a}$$

In our test problems, the constant cross section scheme (CXS DFEM) uses the average of $\Sigma_t(s)$ to generate $\hat{\Sigma}_t$:

$$\hat{\Sigma}_t = \frac{1}{2} \int_{-1}^{1} \Sigma_t(s) \, ds. \tag{3.22}$$

3.2.2 Self-Lumping Quadrature Integration

Schemes that are self-lumping evaluate the integrals of Eqs. (3.15)-(3.20) using numerical quadrature. By definition, self-lumping schemes create diagonal reaction and mass matrices:

$$\mathbf{R}_{\Sigma_t,ij} = \begin{cases} w_i \Sigma_t(s_i) & i = j \\ 0 & \text{otherwise} \end{cases} \tag{3.23a}$$

$$\mathbf{M}_{ij} = \begin{cases} w_i & i = j \\ 0 & \text{otherwise} \end{cases}. \tag{3.23b}$$

Though the choice of interpolation points does not affect exact integration schemes, as shown in [16], the choice of interpolation points was shown to influence both the robustness and accuracy of self-lumping schemes. We consider equally-spaced closed Newton-Cotes, Lobatto-Gauss-Legendre, and Gauss-Legendre quadratures as interpolation points for self-lumping schemes.

We now briefly highlight the attributes of each self-lumping scheme. Methods are referred to by their shorthand notations, given in Table 2.1. In a homogeneous, source-free, purely absorbing medium, SLXS Newton-Cotes yields a strictly positive angular flux outflow for all odd degree polynomial trial spaces. SLXS Newton-Cotes in general does not exactly integrate $\mathbf{L}$ or $\mathbf{M}$. SLXS Lobatto always exactly integrates $\mathbf{L}$, always approximates $\mathbf{M}$, and yields strictly positive angular flux outflows in a source-free pure absorber with constant cross section for all odd degree polynomial trial spaces. SLXS Gauss always exactly integrates both $\mathbf{L}$ and $\mathbf{M}$, and has a strictly positive outflow angular flux in a constant cross section, source-free pure absorber for all even degree polynomial trial spaces. For additional information regarding mass matrix lumping and self-lumping techniques for DFEM S_N transport in homogeneous media, the interested reader is referred to [16]. We do not expect any self-lumping

scheme to exactly integrate $\mathbf{R}_{\Sigma_t}$, as the integrand defining $\mathbf{R}_{\Sigma_t}$ will generally not be a polynomial.

3.3   Pure Absorber Numerical Results

A beam of radiation, $\psi_{in}(\mu_d)$, is incident on the left face of the slab, the right face is a vacuum boundary, $x \in [0, x_R]$, and there are no fixed volumetric sources in the medium. We consider $\Sigma_t(x)$ to be of the form,

$$\Sigma_t(x) = c_1 e^{c_2 x} , \tag{3.24}$$

with c_1 and c_2 are constants $[cm^{-1}]$, with $c_1 > 0$ and $c_2 \neq 0$. The analytic angular flux solution for a source-free pure absorber with an exponentially varying cross section is:

$$\psi(x, \mu) = \begin{cases} \psi_{in}(\mu) \exp\left[\frac{c_1}{\mu c_2} \left(1 - e^{c_2 x}\right) \right] & \mu = \mu_d \\ 0 & \text{otherwise} \end{cases} . \tag{3.25}$$

By definition, the outflow angular flux from cell i, $\psi_{out,i}$ is $\psi(x_{i+1/2}, \mu_d)$ and the average angular flux within cell i, $\psi_{A,i}$ as

$$\psi_{A,i} = \frac{1}{\Delta x_i} \int_{x_{i-1/2}}^{x_{i+1/2}} \psi(x, \mu_d) \ dx , \tag{3.26}$$

with $\Sigma_t(x)$ defined as in Eq. (3.24). The analytical average flux value is:

$$\psi_{A,i} = \frac{\psi_{in}(\mu_d)}{\Delta x_i} \exp\left[\frac{c_1}{\mu_d c_2} \right] \left[E_1\left(\frac{c_1 e^{c_2 x_{i+1/2}}}{\mu_d c_2} \right) - E_1\left(\frac{c_1 e^{c_2 x_{i-1/2}}}{\mu_d c_2} \right) \right] , \tag{3.27}$$

with E_1 the exponential integral [1].

54

The only variable cross-section schemes that yields strictly positive angular outflows in a source-free pure absorber are the SLXS Lobatto and SLXS Newton-Cotes schemes using a linear trial space. For $\mu_d > 0$, consider a source-free, purely absorbing cell with known inflow, $\psi_{in}(\mu_d)$, of width Δx, and the total cross section at each interpolation point is $\Sigma_{t,j}$. Regardless of the actual functional form of the cross section within the cell, the linear DFEM SLXS Lobatto and SLXS Newton-Cotes schemes' numerical angular flux outflow, $\widetilde{\psi}_d(1)$, is:

$$\widetilde{\psi}_d(1) = \frac{2\mu_d^2 \psi_{in}(\mu_d)}{2\mu_d^2 + \Delta x^2 \Sigma_{t,1}\Sigma_{t,2} + \Delta x \mu_d \Sigma_{t,1} + \Delta x \mu_d \Sigma_{t,2}} . \tag{3.28}$$

Equation 3.28 is strictly positive when $\Sigma_t(x) \geq 0$, suggesting that the strictly positive outflow results observed in [16] might hold for an arbitrarily varying spatial cross section. However, the results of [16] do not hold for higher-order DFEM approximations for spatially dependent cross sections.

To demonstrate that negative cell outflows are possible, we carry out the following test. In Fig. ??, we plot the angular flux outflow of each method as a function of trial space degree, and the parameter c_2. We hold the total cell optical thickness to 20 mean-free-path (MFP), vary $c_2 \in [1, 10]$, fix $x_R = 1$, and $\mu_d = 1$. With an exponential cross section, the cell optical thickness in MFP of a cell with $x \in [0, x_R]$ is:

$$MFP = \int_0^{x_R} \Sigma_t(x) \ dx = \frac{c_1}{c_2} \left(e^{c_2 x_R} - 1 \right) . \tag{3.29}$$

To maintain a constant optical thickness in Fig. ??, c_1 is required to be:

$$c_1 = \frac{c_2 \ MFP}{e^{c_2 x_R} - 1} . \tag{3.30}$$

Figure **??** confirms that SLXS Lobatto (and the equivalent SLXS Newton-Cotes scheme) with a linear trial space is the only scheme that explicitly accounts for the spatial variation of cross and maintains a strictly positive angular flux outflow regardless of the shape of $\Sigma_t(x)$. From Fig. **??** we also observe that $\widetilde{\psi}_{out}$ varies for every method as a function of the shape of $\Sigma_t(x)$, with the obvious exception of CXS DFEM. Considering that the analytic angular flux outflow is only a function of total cell MFP:

$$\psi_{out,i} = \psi_{in}(\mu_d) \exp\left[-\int_0^{x_{i+1/2}} \Sigma_t(x) \, dx / \mu_d\right] = \psi_{in}(\mu_d) \exp\left[-MFP \, / \mu_d\right], \quad (3.31)$$

it is unphysical and undesirable that $\widetilde{\psi}_{out}$, for the SLXS Gauss, SLXS Lobatto, SLXS Newton-Cotes, and EXS DFEM schemes, depends on the spatial shape of $\Sigma_t(x)$.

3.3.2 Multiple Cell Spatial Convergence Rates

We now consider the order of spatial convergence for the following schemes: CXS DFEM, SLXS Gauss, SLXS Lobatto, and SLXS Newton-Cotes. Since exact integration of $\mathbf{R}_{\Sigma_t}$ is generally not feasible, we no longer consider the EXS DFEM scheme. Convergence results of the following angular flux errors as a function of the polynomial approximation order are presented:

$$E_\psi = \sqrt{\sum_{i=1}^{N_{cells}} \int_{x_{i-1/2}}^{x_{i+1/2}} \left(\widetilde{\psi}_d(x) - \psi(x, \mu_d)\right)^2 \, dx} \qquad (3.32a)$$

$$E_{\psi_A} = \sqrt{\sum_{i=1}^{N_{cells}} \Delta x_i \left(\widetilde{\psi}_{A,i} - \psi_{A,i}\right)^2} \qquad (3.32b)$$

$$E_{\psi_{out}} = \sqrt{\sum_{i=1}^{N_{cells}} \Delta x_i \left(\widetilde{\psi}_{out,i} - \psi(x_{i+1/2}, \mu_d)\right)^2}. \qquad (3.32c)$$

56

In Eqs. (3.32), Δx_i is the width of cell i, cell i spans $[x_{i-1/2}, x_{i+1/2}]$, $\widetilde{\psi}_d(x)$ is the DFEM numerical approximation, $\psi(x, \mu_d)$ is the analytic solution (see Eq. (3.25)). The problem is spatially discretized using N_{cells} spatial cells of equal width. We approximate the integrals defining the L^2 norm of the angular flux error, E_ψ, using a high-order Gauss quadrature set, $(w_{f,q}, s_{f,q})$, with N_{qf} points, such that:

$$\int_{x_{i-1/2}}^{x_{i+1/2}} \left(\widetilde{\psi}(x) - \psi(x, \mu_d) \right)^2 \, dx \approx \frac{\Delta x_i}{2} \sum_{q=1}^{N_{qf}} w_{f,q} \left(\widetilde{\psi}(s_{f,q}) - \psi(s_{f,q}, \mu_d) \right)^2 . \quad (3.33)$$

For the results that follow, $N_{qf} = 10$. We recall the definitions for the numerical approximations of the cell average angular flux, $\widetilde{\psi}_{A,i}$, and the outflow angular flux, $\widetilde{\psi}_{out,i}$:

$$\widetilde{\psi}_{A,i} = \frac{1}{2} \sum_{j=1}^{N_P} w_j \psi_{i,j} \quad (3.34a)$$

$$\widetilde{\psi}_{out,i} = \sum_{j=1}^{N_P} \psi_{i,j} b_j(1) . \quad (3.34b)$$

We also consider the convergence of the numerical interaction rate, $\widetilde{IR}(x)$ to the true interaction rate $IR(x)$. First, we define the analytic reaction rate for our beam problem:

$$IR(x) = \Sigma_t(x)\psi(x, \mu_d) . \quad (3.35)$$

Similarly, we define a cell average interaction rate as:

$$IR_{A,i} = \frac{1}{\Delta x_i} \int_{x_{i-1/2}}^{x_{i+1/2}} \Sigma_t(x)\psi(x, \mu_d) \, dx . \quad (3.36)$$

Defining a point-wise numerical approximation, $\widetilde{IR}(x)$, to the analytic interaction

rate for the self-lumping schemes presents a unique problem, since only a a numerical quadrature is used to approximate the integrand of **R**. Quadrature integration only requires point evaluations of $\Sigma_t(x)$, not knowledge of $\Sigma_t(x)$ in between quadrature points. However, for the purpose of plotting the SLXS schemes, we define:

$$\widetilde{IR}(s) = \sum_{j=1}^{N_P} b_j(s)\psi_{j,d}\Sigma_t(s_j) \,. \tag{3.37}$$

It must be emphasized that Eq. (3.37) is only used for plotting purposes. We approximate the cell average interaction rate in cell i as:

$$\widetilde{IR}_{A,i} = \frac{1}{2} \sum_{j=1}^{N_P} w_j \Sigma_t(s_j)\psi_{j,d} \,. \tag{3.38}$$

In Eq. (3.38), $\Sigma_t(s_j) = \hat{\Sigma}_t$ for the CXS DFEM scheme, and $\Sigma_t(s_j)$ is the point evaluation of the true cross section for all other schemes.

We consider two measures to assess the error of the DFEM schemes' approximation of the true interaction rate, $IR(x)$. The first, E_{IR} is an approximation of the L^2 norm of interaction rate error:

$$E_{IR} = \sqrt{\sum_{i=1}^{N_{cells}} \frac{\Delta x_i}{2} \sum_{q=1}^{N_P} w_q \left(IR(s_q) - \Sigma_t(s_q)\widetilde{\psi}(s_q, \mu_d) \right)^2} \,. \tag{3.39}$$

We reiterate that, for the self-lumping schemes, $\widetilde{IR}(s)$ is only truly defined at the DFEM interpolation points. E_{IR_A} measures the convergence of the average interaction rate:

$$E_{IR_A} = \sqrt{\sum_{i=1}^{N_{cells}} \Delta x_i (IR_{A,i} - \widetilde{IR}_{A,i})^2} \,. \tag{3.40}$$

For our convergence study, we consider a source-free purely absorbing slab with

a cross section that varies exponentially in space as in Eq. (3.24) with $c_1 = 0.1$ and $c_2 = 2\ln(10)$. A beam of radiation is incident on the left face in the direction of $\mu_d = 1$, vacuum boundary conditions exist on the right face of the slab, and $x \in [0, 1]$. The convergence of the E_ψ, E_{ψ_A}, and $E_{\psi_{out}}$ as a function of the choice of numerical scheme and trial space polynomial degree are given in Fig. **??**, Fig. **??**, and Fig. **??**, respectively. Convergence of E_{IR} and E_{IR_A} as function of numerical scheme and trial space polynomial degree are given in Fig. **??** and Fig. **??**. The plateauing of numerical errors for various high-order methods using very small cell sizes in Figs. **??**-**??** is a consequence of having reached machine precision. The lines in Figs. **??**-**??** that extend to values smaller than machine precision are reference lines.

Figures **??**-**??** show that, for a linear angular flux trial space, CXS DFEM achieves the same orders of spatial convergence as observed with Exact DFEM in [16]. However, as the degree of the DFEM trial space is increased, the CXS DFEM scheme does not show an increase in the order of the spatial convergence rate of E_ψ and E_{ψ_A}; the convergence rate of CXS DFEM is limited to at most second order for both E_ψ and E_{ψ_A}, regardless of the trial space polynomial degree. The increase in order of convergence of CXS DFEM for $E_{\psi_{out}}$ as trial space is increased is a result of angular flux outflow in the CXS DFEM discretization being only a function of the cell optical thickness, which is preserved exactly by our definition of $\hat{\Sigma}_t$; see Eq. (3.22).

Of the self-lumping schemes, SLXS Newton-Cotes is the least accurate. SLXS Newton-Cotes convergence of E_ψ is limited to at most second order for odd degree polynomial trial spaces and third order for even degree trial spaces. Convergence of E_{ψ_A} and $E_{\psi_{out}}$ for the SLXS Newton-Cotes scheme generally increases with an increase in the DFEM polynomial trial space degree, but is only proportional to P.

Both SLXS Lobatto and SLXS Gauss converge E_ψ, E_{ψ_A}, and $E_{\psi_{out}}$ similarly to the study carried out in [16] with a spatially constant cross section. The spatial

convergence of E_ψ for SLXS Lobatto and SLXS Gauss is order $P + 1$. Though SLXS Lobatto and SLXS Gauss converge with the same order of spatial convergence for E_ψ, SLXS Gauss is more accurate than SLXS Lobatto by a constant. SLXS Gauss converges E_{ψ_A} and $E_{\psi_{out}} \propto 2P + 1$, whereas SLXS Lobatto converges both $\propto 2P$. SLXS Gauss and SLXS Lobatto converge angular flux error quantities for the case of a spatially varying cross section with the same rates of convergence as their constant cross-section analogs did in [16]. This suggests that exactly integrating the interaction term in the DFEM moment equations is not essential for developing arbitrarily high-order accuracy DFEM schemes for radiation transport.

We observe the detrimental effect of approximating a spatially varying cross section with a constant in each spatial cell when we examine the L_2 convergence results for the interaction rate, E_{IR}, for the CXS DFEM scheme. Regardless of angular flux trial space polynomial degree, CXS DFEM converges E_{IR} to only first order in space. However, the self-lumping schemes exhibit the same trends in converging E_{IR} (in the L^2-norm sense) as exhibited in converging E_ψ:

- SLXS Lobatto and SLXS Gauss converge E_{IR} with order $P + 1$,

- SLXS Gauss is more accurate than SLXS Lobatto by a constant, and

- SLXS Newton-Cotes converges E_{IR} second order in space for odd degree trial spaces and third order in space for even degree trial spaces.

The convergence results of the cell average interaction rate, E_{IR_A}, shown in Fig. **??**, do not behave as intuitively. Given the poor performance of CXS DFEM in converging E_{IR}, one would expect that CXS DFEM would converge E_{IR_A} poorly as well. However, this is not the case and CXS DFEM converges E_{IR_A} with the same order of convergence as the best performing self-lumping scheme considered.

60

CXS DFEM converges E_{IR_A} with a high-order of accuracy because of the locally conservative properties of DFEM approximations, that is:

Particles Into Cell − Particles Out of Cell = Total Interactions in Cell . (3.41)

As shown in Fig. **??**, CXS DFEM converges the quantities on the left hand side of Eq. (3.41) with the same order of accuracy as any self-lumping scheme considered; CXS DFEM is at least as accurate in calculating the particles into a cell (outflow from the previous cell) and out of the cell (outflow from the current cell) as any other scheme considered. Since Eq. (3.41) holds regardless of the numerical scheme considered, it follows that CXS DFEM converges E_{IR_A}, the term in the right hand side of Eq. (3.41) summed over all cells, with the maximum order of convergence displayed by any of the DFEM schemes we consider here. Fig. **??** validates this conclusion. CXS DFEM and SLXS Gauss exhibit the highest order of spatial convergence, converging E_{IR_A} with order $\propto 2P + 1$. SLXS Newton-Cotes and SLXS Lobatto converge E_{IR_A} with the same orders of convergence each method exhibits in converging E_{ψ_A} for this problem with SLXS Lobatto converging $\propto 2P$ and SLXS Newton-Cotes $\propto P$.

3.3.3   Consequences of Assuming a Cell-Wise Constant Cross Section

To understand the poor convergence of point-wise error in angular flux and interaction rate, E_ψ and E_{IR}, associated with CXS DFEM we now examine more closely the CXS DFEM spatial approximations to $\psi(x, \mu_d)$ and $IR(x)$. We again consider a pure absorber with total absorption cross section that varies exponentially in space with $c_1 = 0.1$, and $c_2 = 2 \ln(10)$. A beam of radiation is incident on the left face in the direction of $\mu_d = 1$, vacuum boundary conditions are applied on the right face of the slab, and $x \in [0, 1]$.

In Fig. **??**, we plot the exact $\psi(x)$ and $IR(x)$, as well as their CXS DFEM

61

numerical approximations, $\widetilde{\psi}(x)$ and $\widetilde{IR}(x)$, using $N_{cells} = 5$, and $\hat{\Sigma}_{t,i}$ as defined in Eq. (3.22). Additionally, we plot the analytic angular flux and reaction rate one would obtain if the cell average cross section, $\hat{\Sigma}_{t,i}$, had been used instead of the true $\Sigma_t(x)$. We refer to these analytic solutions as $\psi_C(x)$ and $IR_C(x)$.

Since CXS DFEM is a discontinuous scheme, some discontinuity is expected in the plots of $\widetilde{\psi}$ and $\widetilde{IR}$ in Fig. **??**. However, the discontinuities present in $\widetilde{IR}(x)$ of Fig. **??** are highly disconcerting. The analytic $IR(x)$ is smooth and does not vary rapidly within individual mesh cells, yet there are significant, non-monotonic discontinuities in the CXS DFEM interaction rate solution to the pure absorber problem with exponentially varying cross section. The noticeably poor behavior of $\widetilde{IR}(x)$ in Fig. **??** is inherent to the assumption of a cell-wise constant cross section. This is clearly visible in Fig. **??** when $\psi(x)$ and $IR(x)$, calculated assuming a spatially varying cross section, are compared to the analytic solutions assuming a cell average cross section, $\psi_C(x)$ and $IR_C(x)$. Figure **??** does not suggest that linear DFEM is unsuitable for use in problems with spatially varying cross sections. Rather, comparing the CXS DFEM $\widetilde{\psi}(x)$ and $\widetilde{IR}(x)$ to $\psi_C(x)$ and $IR_C(x)$ in Fig. **??**, we see that CXS DFEM is very accurate when the problem is assumed to have piece-wise constant, cell averaged cross sections.

Given the poor accuracy of CXS DFEM in approximating the true $\psi(x)$ and $IR(x)$, consider $\widetilde{\psi}(x)$ and $\widetilde{IR}(x)$ obtained with SLXS Lobatto using a linear DFEM trial space and five spatial cells, shown in Fig. **??**, for the same problem. In Fig. **??**(a), the differences between the angular flux solutions obtained using (1) a cell-wise constant cross section (CXS DFEM) and (2) evaluating cross section values at quadrature points (SLXS Lobatto) are small. This is not the case when comparing the different approximations to the interaction rate, $\widetilde{IR}(x)$, in Fig. **??**(b). Though there are discontinuities in the SLXS Lobatto $\widetilde{IR}(x)$, the discontinuities are smaller and

the SLXS Lobatto $\widetilde{IR}(x)$ is monotonic unlike the CXS DFEM $\widetilde{IR}(x)$. The SLXS Lobatto $\widetilde{IR}(x)$ is clearly more accurate than the CXS DFEM $\widetilde{IR}(x)$. In this problem, there are two possible sources of error that could cause a DFEM to be inaccurate: inexact matrix evaluation and not incorporating cross-section spatial variation into the scheme. By definition, CXS DFEM exactly integrates the mass matrix, and we showed in [16] that schemes which exactly integrate the mass matrix are more accurate than schemes that only approximately integrate the mass matrix, like SLXS Lobatto. Thus, the poor accuracy of CXS DFEM relative to SLXS Lobatto is entirely caused by the approximation of a spatially varying cross section with a cell-wise constant value.

The "blading" in $\widetilde{IR}(x)$ has not previously been reported in the radiation transport literature. We are likely not the first to have generated these large, non-monotonic discontinuities. In fact, we believe that blading has frequently been present in DFEM radiation transport simulations and literature, but has likely gone unnoticed due to the prevalence of linear DFEM and simplified data visualization using cell midpoint values. Consider Fig. **??**(a) and Fig. **??**(b) that linearly interpolate between $\widetilde{\psi}_{A,i}$ and $\widetilde{IR}_{A,i}$ plotted at cell centers. While Fig. **??**(a) is visually indistinguishable from Fig. **??**(a), the blading of $\widetilde{IR}(x)$ present in Fig. **??**(b) is not at all visually present in Fig. **??**(b).

Interaction rate terms are present in other radiation transport physics. In particular, we think of the radiative transfer analog to the neutronics interaction rate, absorption rate density.

3.3.4   Flux-Weighting versus Volume-Averaged Cross Sections

In our results thus far, we have only considered volume-averaged cell-wise cross sections(the CXS DFEM scheme). However, in reactor physics problems, a flux-

weighted cross section is often used to generate spatially averaged cross sections [**?**]. We now introduce the flux-weighted cell-wise constant cross section scheme (FW CXS), which differs from the CXS DFEM scheme only by how $\hat{\Sigma}$ is defined in each cell:

$$\hat{\Sigma}_i = \frac{\int_{x_{i-1/2}}^{x_{i+1/2}} \Sigma(x)\psi(x,\mu_d)\ dx}{\int_{x_{i-1/2}}^{x_{i+1/2}} \psi(x,\mu_d)\ dx} \ . \tag{3.42}$$

In practice, flux-weighting is often done using the scalar flux in order not to have angle-dependent total cross section. However for the beam problem considered here, $\psi(x,\mu_d)$ is proportional to the scalar flux.

We first compare the accuracy of FW CXS versus volume-averaged CXS DFEM for a cubic DFEM trial space, as shown in Fig. **??**. Figure **??** shows that FW CXS scheme is more accurate than CXS DFEM when comparing E_ψ, E_{ψ_A} and, at low resolutions, for E_{IR}. However, though designed to preserve cell average interaction rates, FW CXS scheme is not only less accurate than CXS DFEM in calculating cell average interaction rates, it converges at most second order in space, whereas a volume-averaged cross section converges $\propto 2P + 1$ for the pure absorber problem.

Finally, we consider the $\widetilde{\psi}_d(x)$ and $\widetilde{IR}(x)$ solution representations of the FW CXS scheme. In Fig. **??** it is clear that while the FW CXS and CXS DFEM schemes calculate slightly different solution representations, the FW CXS scheme exhibits the same interaction rate blading phenomena as the CXS DFEM scheme, reiterating that blading is a result of approximating a spatially varying cross section with as a cell-wise constant. The choice of cell-wise cross section does not eliminate blading.

3.3.5   Effects of Mesh Spacing

In practice, computational domains are not necessarily discretized with uniform grids; rather cells are concentrated in regions where the solution is known or assumed to vary rapidly. For the pure absorber problem, we compare two alternative methods

of mesh spacing (logarithmic grids and equal optical thickness grids, see Table **??**),
to the results obtained with equally-spaced mesh cells. We derive how to generate
these meshes in Section **??** and give results in Section 3.3.5.2

3.3.5.1   Generating Improved Spatial Meshes

Two alternative meshing strategies are compared to equally-spaced meshed. In
the following, we will use a shorthand notation, given in Table **??**. With the MFP
meshing strategy, we find each cell width by determining the width of each cell from
$i = 1$ (leftmost cell) to $i = N_{cell}$ as outlined by Eq. (3.43): First, we determine the
average cell optical thickness:

$$\bar{h} = \frac{\int_{x_{1/2}}^{x_{N_{cell}+1/2}} \Sigma_t(x) \ dx}{N_{cell}} \ . \tag{3.43a}$$

Then, we solve the following equation for $x_{i+1/2}$:

$$\int_{x_{i-1/2}}^{x_{i+1/2}} \Sigma_t(x) \ dx - \bar{h} = 0 \ , \tag{3.43b}$$

yielding

$$x_{i+1/2} = \frac{1}{c_2} \log \left[\frac{c_2(\bar{h} + \Sigma_t(x_{i-1/2}))}{c_1} \right] \ . \tag{3.43c}$$

There are several ways to specify LOG spacing, but we elected to set a ratio, 0.6,
between adjacent cell sizes with the caveat that we would set a minimum cell size,
Δx_{min}. In our convergence testing, at the first refinement when $\Delta x_{N_{cell}} < \Delta x_{min}$, the
grid is "fixed" and all further refinements uniformly refine the "fixed" grid. $\Delta x_{N_{cell}}$
is the cell width for the right most cell where, for $R < 1$,

$$\Delta x_i = \Delta x_1 R^{i-1}, \ i \in [1, N_{cell}] \ . \tag{3.44}$$

Δx_1 is determined by requiring that the geometric series of cell widths completely fill the space:

$$\Delta x_1 = \left(x_{N_{cell}+1/2} - x_{1/2}\right) \frac{1-R}{1-R^{N_{cell}}} \qquad (3.45)$$

The grid is "fixed" by resetting the width of every cell whose width, if set to the value required for a purely logarithmically spaced grid with R would be below Δx_{min}, to Δx_{min}. After imposing this, cell widths are determined by requiring the cells that were not reset to fill the problem space logarithmically using R. If there is no minimum cell width, at high mesh refinements, most cells will be infinitesimally small and the large cells will never be refined, causing error to stagnate. Logarithmic spacing represents the "smart" meshing strategy most likely to be employed in engineering practice as it requires the least amount of solution information prior to problem execution. For all of our calculations, we set $R = 0.6$ and $\Delta x_{min} = 10^{-3} \, [cm]$.

First, we note that the choice of mesh spacing method does not alter asymptotic convergence rates, as shown in Fig. **??**. Figure **??** shows that the SLXS Lobatto scheme with a quadratic trial space converges E_ψ, E_{ψ_A}, E_{IR}, and E_{IR_A} at the same asymptotic rate, regardless of grid spacing choice. Plots showing other trial space degrees and DFEM schemes are omitted for brevity. We also omit showing the convergence of $E_{\psi_{out}}$ as we have already demonstrated that the convergence rate of $E_{\psi_{out}}$ and E_{IR_A} are related and identical.

At mesh refinements that are not in the asymptotic convergence regime, the selection of a smart meshing methodology can result in a significant reduction in error. Consider Fig. **??**, Fig. **??**, and Fig. **??** that show the values of E_ψ, E_{ψ_A}, E_{IR}, and E_{IR_A} for the SLXS Lobatto, SLXS Gauss, and CXS DFEM schemes respectively for a quadratic trial space. First, we note that any particular mesh spacing methodology results in solutions that are more accurate for certain quantities, but not for all

quantities. For example, with the self-lumping schemes, E_ψ is generally smaller when using an equally spaced mesh, but using the LOG mesh results in orders of magnitude improvement in E_{IR} and E_{IR_A} on coarse meshes. In Fig. **??**, CXS DFEM again illustrates that LOG spacing is more accurate in calculating interaction rate quantities than an equally-spaced mesh and equally-spaced meshes are generally more accurate than other meshing strategies for calculating angular flux quantities. However, CXS DFEM shows a two order of magnitude reduction in calculating E_{IR_A} when using a mesh that has a uniform optical thickness in each cell. This is a direct result of CXS DFEM converging as $\hat{\sigma}\Delta x \to 0$.

3.3.5.2 Mesh Spacing Results

The important results from Figs. **??-??** are summarized here:

1. mesh spacing does not affect asymptotic order of convergence,

2. accuracy in calculating certain quantities of interest (point-wise and cell averaged reaction rates) is improved with alternative meshing strategies at low resolution.

4. LAST CHAPTER: THE IMPORTANCE OF RESEARCH

4.1 New Section

5. LAST CHAPTER: THE IMPORTANCE OF RESEARCH

5.1   New Section

6. LAST CHAPTER: THE IMPORTANCE OF RESEARCH

6.1   New Section

REFERENCES

[1] M. Abramowitz and I. A. Stegun. *Handbook of Mathematical Functions with Formulas, Graphs, and Mathematical Tables.* United States Department of Commerce, Washington, D.C., 1972.

[2] M. L. Adams. Subcell balance methods for radiative transfer on arbitrary grids. *Transport Theory and Statistical Physics*, 26(4 &5):385–431, 1997.

[3] M. L. Adams. Discontinuous finite element transport solutions in thick diffusive problems. *Nuclear Science and Engineering*, 137:298–333, 2001.

[4] M. L. Adams and P. F. Nowak. Asymptotic analysis of a computational method for time- and frequency- dependent radiative transfer. *Journal of Computational Physics*, 46:366–403, 1998.

[5] R. Alexander. Diagonally implicit runge-kutta methods for stiff o.d.e.'s. *SIAM Journal of Numerical Analysis*, 14(6):1006–1021, 1977.

[6] S. Hamilton ans M. Benzi and J. S. Warsa. Negative flux fixups in discontinuous finite elements sn transport. In *International Conference on Mathematics, Computational Methods & Reactor Physics*, Saratoga Springs, New York, May 2009.

[7] J. P. Hennart and E. del Valle. A generalize nodal finite element formalism for discrete ordinate equations in slab geometry: Part ii theory in the discontinuous moment case. *Transport Theory and Statistical Physics*, 24:479–504, 1995.

[8] J. P. Hennart and E. del Valle. A generalize nodal finite element formalism for discrete ordinate equations in slab geometry: Part iii numerical results. *Transport Theory and Statistical Physics*, 24:505–533, 1995.

[9] A. Kavenoky and J. Lautard. A finite element depletion diffusion calculation method with space-dependent cross section. *Nuclear Science and Engineering*, 64(2):563–575, 1977.

[10] E. W. Larsen and W. F. Miller. Convergence rates of spatial difference equations for the discrete-ordinates neutron transport equations in slab geometry. *Nuclear Science and Engineering*, 73:76–83, 1980.

[11] E. W. Larsen and J. E. Morel. Asymptotic solutions of numerical transport problems in optically thick, diffusive regimes ii. *Journal of Computational Physics*, 83:212–236, 1989.

[12] E. W. Larsen and P. Nelson. Finite-difference approximations and superconvergence for the discrete ordinates equations in slab geometry. *SIAM Journal of Numerical Analysis*, 19(2):334–348, 198.

[13] K. D. Lathrop. Spatial differencing of the transport equation: Positivity vs. accuracy. *Journal of Computational Physics*, 4:475–498, 1969.

[14] E. E. Lewis and W. F. Miller. *Computational Methods of Neutron Transport*. American Nuclear Society, La Grange Park, IL, 1993.

[15] P. G. Maginot, J. E. Morel, and J. C. Ragusa. A non-negative moment preserving spatial discretization scheme for the linearized boltzmann transport equation in 1-d and 2-d cartesian geometries. *Journal of Computational Physics*, 231(20):6801–6826, 2012.

[16] P. G. Maginot, J. C. Ragusa, and J. E. Morel. Lumping techniques for dfem transport in s_n transport in slab geometry. *Nuclear Science and Engineering*, 179(2):148–163, 2015.

[17] The MathWorks. Matlab 2011b, 2011.

[18] J. E. Morel, T. A. Wareing, and K. Smith. A linear-discontinuous spatial differencing scheme for s_n radiative transfer calculations. *Journal of Computational Physics*, 128:445–462, 1996.

[19] J. E. Morel, T.-Y. B. Yang, and J. S. Warsa. Linear multifrequency-grey acceleration recast for preconditioned krylov iterations. *Journal of Computational Physics*, 227:244–264, 2007.

[20] C. C. Ober and J. N. Shadid. Studies on the accuracy of time-integration methods for the radiation-diffusion equations. *Journal of Computational Physics*, 195:743–772, 2004.

[21] P. A. Raviart. The use of numerical integration in finite element methods for solving parabolic equations. In *Conference on Numerical Analysis, RIANA 1972*, pages 233–264, August 1972.

[22] W. H. Reed, T. R. Hill, F. W. Brinkley, and K. D. Lathrop. Triplet: A two-dimensional, multigroup, triangular mesh, planar geometry, explicit transport code. Technical Report LA-5428-MS, Los Alamos Scientific Lab, 1973.

[23] K. Salari and P. Knupp. Code verification by the method of manufactured solutions. Technical Report SAND2000-1444, Sandia National Labs, 2000.

[24] S. Santandrea and P. Bellier. An unstructured characteristics scheme with a linear expansion for both fluxes and cross sections. In *Proceedings of the Joint International Topical Meeting on Mathematics & Computation and Supercomputing in Nuclear Applications (M&C + SNA 2007)*, Monterey, California, April 2007.

[25] W. M. Stacey. *Nuclear Reactor Physics*. John-Wiley & Sons Inc., 2001.

[26] B. Su and G. L. Olson. An analytical benchmark for non-equilibrium radiative transfer in an isotropically scattering medium. *Annals of Nuclear Engergy*, 24(13):1035–1055, 1997.

[27] V. Thomee. *Galerkin Finite Element Methods for Parabolic Problems*. Springer, New York, 1997.

[28] W. F. Walters. The relation between finite element methods and nodal methods in transport theory. *Progress in Nuclear Energy*, 18:21–26, 1986.

[29] Y. Wang and J. C. Ragusa. A high-order discontinuous galerkin method for the sn transport equations on 2d unstructured triangular meshes. *Annals of Nuclear Energy*, 36(7):931–939, 2009.

[30] Y. Wang and J. C. Ragusa. On the convergence of dgfem applied to the discrete ordinates transport equation for structured and unstructured triangular meshes. *Nuclear Science and Engineering*, 163:56–72, 2009.

[31] J. S. Warsa and A. K. Prinja. p-adaptive numerical methods for particle transport. *Transport Theory and Statistical Physics*, 28(3):229–270, 1999.

[32] J. S. Warsa, T. A. Wareing, and J. E. Morel. Krylov iterative methods and the degraded effectiveness of diffusion synthetic acceleration for multidimensional s_n calculations in problems with material discontinuities. *Nuclear Science and Engineering*, 147(3):218–248, 2004.

APPENDIX A

FIRST APPENDIX

Text for the Appendix follows.

Figure A.1: TAMU figure

APPENDIX B

SECOND APPENDIX WITH A LONGER TITLE - MUCH LONGER IN FACT

Text for the Appendix follows.

B.1   Appendix Section

Figure B.1: TAMU figure